

How does a MOND cosmology fare on Gpc scales? – Collisionless N -body simulations of ν HDM

Alfie Russell^{1*}, Indranil Banik^{2,1}, Oscar Cray¹ and Hongsheng Zhao^{1,3}

¹Scottish Universities Physics Alliance, University of Saint Andrews, North Haugh, Saint Andrews, Fife, KY16 9SS, UK

²Institute of Cosmology and Gravitation, University of Portsmouth, Dennis Sciamia Building, Burnaby Road, Portsmouth PO1 3FX, UK

³Department of Astronomy, School of Physical Sciences, University of Science and Technology of China, Hefei, Anhui 230026, China

Accepted XXX. Received YYY; in original form ZZZ

ABSTRACT

We present the largest collisionless N -body cosmological simulations in a Modified Newtonian Dynamics (MOND) cosmology to date. Our 4 simulations cover Λ CDM as a baseline, a MOND with hot dark matter model known as ν HDM, and 2 unphysical models we call Λ HDM and ν CDM to test the individual contributions of hot dark matter and MOND gravity, respectively. ν HDM reproduces the CMB power spectrum whilst also theoretically matching cluster dynamics and preserving MOND predictions for galactic rotation curves. We test its viability on cosmological scales using simulations with 256^3 particles in a box of size $800/h$ comoving Mpc. We find generically that the MOND models massively overproduce large-scale structures by $z = 0$, with a most massive cluster in ν HDM of $\approx 5 \times 10^{17} M_{\odot}/h$ and typical peculiar velocities of several thousand km/s. We also explore a local void solution to the Hubble tension in these models. Analogues to the observed “Local Hole” do form in the MOND models, but values for the deceleration parameter < -1.5 in these regions prevent a satisfactory resolution to the Hubble tension. Whilst Λ CDM significantly underpredicts the observed bulk flow in Cosmicflows-4, the high peculiar velocities that arise in the MOND models create the opposite problem, ruling out ν HDM at $> 5\sigma$ confidence. Observations clearly require a much milder enhancement to the rate of structure growth in Λ CDM than is provided by the ν HDM paradigm. Our results also suggest that replacing cold dark matter with hot dark matter is unlikely to provide a viable cosmological model, regardless of the gravity law.

Key words: gravitation – galaxies: clusters: general – cosmology: theory – large-scale structure of Universe – methods: numerical – distance scale

1 INTRODUCTION

A major accomplishment of modern cosmology is an understanding of how structure in the universe grew from small density fluctuations caused by quantum uncertainty in the era of cosmic inflation at very early times (Guth 1981). These fluctuations oscillated in strength prior to recombination due to tight coupling between the baryons and photons at that time, a consequence of the high Thomson scattering cross-section of free electrons. Modes of different wavelengths had different oscillation frequencies, but they all oscillated for a fixed time interval of about 380 kyr between the Big Bang and recombination. This created a characteristic pattern of oscillations in the power spectrum of the Cosmic Microwave Background (CMB; de Bernardis et al. 2000; Hinshaw et al. 2013; Planck Collaboration VI 2020; Atacama Cosmology Telescope collaboration 2025).

In a universe governed by General Relativity (GR; Einstein 1915) with only baryonic matter, the CMB power spectrum would have a very simple form governed purely by diffusion damping, causing each peak to be lower in amplitude than the previous peak

by a similar factor (Hu & Dodelson 2002). This is contrary to the observation that the third peak has a similar amplitude to the second peak, but both have a much lower amplitude than the first peak, violating the expectation that the peak amplitudes decrease in a continuous manner (Spergel et al. 2003, 2007).

Another unusual aspect of the CMB is that once we allow for a dipole anisotropy due to the motion of the Sun relative to the CMB (Kogut et al. 1993), the remaining fluctuations are at the level of 10^{-5} . In linear structure formation theory, the fractional density perturbation $\delta \propto a$ in the era of matter domination, where a is the cosmic scale factor normalized to unity today. The assumption of matter domination is quite accurate because recombination occurred when the universe was $\gtrsim 7\times$ older than at the epoch of matter-radiation equality (Banik & Samaras 2025), while dark energy has only recently become important. Including it only worsens the problem as it slows down structure growth, as does radiation (Meszaros 1974). The temperature fluctuations on the small scales relevant to galaxy formation are smaller still due to diffusion or Silk damping (Silk 1968). Since recombination occurred at redshift $z = 1090$, it is clear that an additional ingredient is required to form gravitationally bound structures on galaxy scales by the present epoch.

In the Λ -Cold Dark Matter (Λ CDM) standard model of cosmology (Efstathiou, Sutherland & Maddox 1990; Ostriker & Stein-

* E-mail: apr8@st-andrews.ac.uk (Alfie Russell);
Indranil.Banik@port.ac.uk (Indranil Banik);
hz4@st-andrews.ac.uk (Hongsheng Zhao)

hardt 1995), the missing ingredient in structure formation theory is CDM. Density perturbations in the CDM could grow as soon as the universe became dominated by matter. The lack of any coupling to radiation allowed these perturbations to grow much more than perturbations in the baryons, which were still very small by the time of recombination.

Besides the issue of structure formation, CDM is also necessary to explain the internal dynamics and stability of many gravitationally bound objects in the local universe. Self-gravitating discs of stars are unstable (Miller & Prendergast 1968; Hockney & Hohl 1969; Hohl 1971), leading to the suggestion of massive dark haloes (Ostriker & Peebles 1973; Ostriker, Peebles & Yahil 1974). These are also necessary to explain why M31 is currently approaching our Galaxy, even though these must have been receding from one another shortly after the Big Bang (the “timing argument”; Kahn & Woltjer 1959). More directly, the internal dynamics of these and other galaxies cannot be explained by their baryonic matter alone (e.g. Rubin & Ford 1970; Rogstad & Shostak 1972; Roberts & Rots 1973; Roberts & Whitehurst 1975; Faber & Gallagher 1979; Mateo 1998; Sofue & Rubin 2001; Tolstoy et al. 2009; Lelli et al. 2016; Simon 2019; Arora et al. 2023). On larger scales, the dynamical masses and X-ray emissions of clusters show they are similarly more massive than their baryonic content (e.g. Zwicky 1933; Biviano 2006; Sereno et al. 2025; Cavaliere & Fusco-Femiano 1976; Pointecouteau & Silk 2005; Etori et al. 2013). This conclusion is further reinforced by measurements of the gravitational field using gravitational lensing by both galaxies and clusters (see Hoekstra & Jain 2008; Natarajan et al. 2024, and references therein). In a Universe governed by GR, a dominant CDM component is a requirement to explain astronomical observations on almost all scales beyond the Solar System.

1.1 Milgromian dynamics (MOND)

Our preceding discussion assumes GR can be extrapolated beyond the Solar System scales for which it was originally designed. The resulting need for dark matter is concerning, as CDM particles would have exotic properties that are not observed for any known particle in the standard model of particle physics. Decades of effort with direct detection experiments have ruled out much of the parameter space originally thought to be viable (LUX Collaboration 2017; Lux-Zeplin Collaboration 2023; Aalbers et al. 2025). Indirect detection experiments give similar conclusions based on over a decade of observations towards the supposedly CDM-dominated dwarf satellites of the Milky Way (Fermi-LAT Collaboration 2015; Hoof et al. 2020; Hu et al. 2024a; Song et al. 2024). These results raise the possibility that CDM particles do not exist.

If disk galaxies are purely baryonic objects, then their visible mass must provide sufficient gravity to explain their observed flat rotation curves, which imply a huge missing gravity problem in the context of GR. Solving this with only the visible mass requires a modification to the dynamical laws. The most widely considered proposal along these lines is known as MOND (Milgrom 1983). The basic idea of MOND is that in an isolated spherically symmetric system with Newtonian gravity g_N , the actual gravity g has the following asymptotic limits:

$$g \rightarrow \begin{cases} g_N, & \text{if } g_N \gg a_0, \\ \sqrt{g_N a_0}, & \text{if } g_N \ll a_0. \end{cases} \quad (1)$$

MOND introduces a_0 as a fundamental new constant of nature with dimensions of acceleration. The idea that gravity should be modified at low accelerations rather than beyond a fixed length was motivated

by the Tully-Fisher relation between flat rotation velocity and galaxy luminosity (Tully & Fisher 1977), which shows that the expected Keplerian decline to the rotation curve becomes anomalously flat at about the same g_N in galaxies of different mass (see sections 2 and 3.1.1 of Banik & Zhao 2022). Galaxy rotation curves require that $a_0 = 1.2 \times 10^{-10} \text{ m/s}^2$ (Begeman, Broeils & Sanders 1991; Gentile, Famaey & de Blok 2011; McGaugh, Lelli & Schombert 2016). For comparison, we do not have direct knowledge of how gravity behaves beyond the 170 AU distance to Voyager 1, our most distant currently operational spacecraft. The gravitational field strength here is $g = 2 \times 10^{-7} \text{ m/s}^2$ or about $1700 a_0$, far higher than typical accelerations in galaxies or in the early universe (see section 3.1.3 of Haslbauer, Banik & Kroupa 2020, hereafter HBK20).

A modification to Newtonian gravity at $g_N \lesssim a_0$ is not only possible, it actually leads to unparalleled predictive success with the rotation curves of galaxies (McGaugh 2020). The MOND prediction of a tight radial acceleration relation (RAR) between g and g_N holds in actual data of galaxies, which show that the intrinsic scatter is $\lesssim 0.034$ dex (Desmond 2023), with residuals from the mean RAR not showing correlations with many properties of galaxies like surface brightness and gas fraction (Stiskalek & Desmond 2023). A similar amount of intrinsic scatter has been inferred using neutral hydrogen observations of a homogeneously analysed sample of 19 galaxies that probe the low-acceleration end of the RAR (Vărășteanu et al. 2025). For comparison, Ludlow et al. (2017) showed that the intrinsic scatter in the RAR in the EAGLE simulations of Λ CDM is 0.08 dex (Crain et al. 2015; Schaye et al. 2015), highlighting that it remains difficult to explain the tight RAR in this paradigm. Moreover, MOND is also successful in elliptical galaxies (Lelli et al. 2017; Chae et al. 2020; Shelest & Lelli 2020) and low surface brightness galaxies (Karukes & Salucci 2017; Di Paolo et al. 2019; McGaugh et al. 2021), where enhanced tidal susceptibility arising from the non-linear behaviour of MOND provides an elegant explanation for the observed signs of disturbance of dwarf galaxies in the Fornax Cluster and the lack of low surface brightness dwarfs towards the cluster centre (Asencio et al. 2022). Developments in stacked galaxy-galaxy weak lensing can now probe g hundreds of kpc from a galaxy in a statistical sense, demonstrating that a tight RAR consistent with the rotation curve data continues to hold at much lower accelerations (about 2.5 dex below a_0 in terms of g or 5 dex in g_N ; Brouwer et al. 2021; Mistele et al. 2024a,b). Relativistic versions of MOND can explain the CMB power spectrum while having gravitational waves that travel at the speed of light (Skordis & Złośnik 2019, 2021, 2022). For extensive reviews of MOND, we refer the reader to Famaey & McGaugh (2012) and Banik & Zhao (2022).

1.2 The neutrino-Hot Dark Matter (ν HDM) model

A long-standing problem with MOND is that it still faces a residual missing gravity problem in galaxy clusters (Sanders 1999, 2003; Pointecouteau & Silk 2005; Eckert et al. 2022; Li et al. 2023, 2024; Kelleher & Lelli 2024; Famaey et al. 2025). It is possible that this problem will be alleviated in a relativistic MOND theory, but this is far from guaranteed (Durakovic & Skordis 2024). If we instead assume that MOND can be applied to galaxy clusters in much the same way as galaxies, we still have to assume that there is some form of undetected mass. This might be in the form of sterile neutrinos with a rest energy of 11 eV, which are the main mass component of the ν HDM paradigm on cluster and larger scales (Angus et al. 2007; Angus 2009; Angus et al. 2010; Wittenburg et al. 2023). The proposed sterile neutrinos are far heavier than ordinary neutrinos,

whose rest energy is at most 0.45 eV (Katrin Collaboration 2019, 2022, 2025). Even so, the low mass of sterile neutrinos would make them a form of HDM – sterile neutrinos with such a low mass would barely affect the MOND fits to galaxy rotation curves (Angus 2010) because their number density is limited by the Pauli Exclusion Principle (the Tremaine-Gunn limit in an astrophysical context; Tremaine & Gunn 1979). However, the larger size and velocity dispersion of galaxy clusters allows for sterile neutrinos to play a greater role, so they can explain the offset between the weak lensing and X-ray peaks in the Bullet Cluster (Angus et al. 2007). Sterile neutrinos can also account for the second and third peaks in the CMB power spectrum having a similar height, provided the sterile neutrinos have about the same average mass density as the CDM in the Λ CDM paradigm (Angus & Diaferio 2011; Samaras, Grandis & Kroupa 2025). This is indeed the case if they are in thermal equilibrium in the early universe. The sterile neutrinos would be non-relativistic at the time of recombination, acting much like CDM. The sterile neutrinos would be relativistic in the era of Big Bang nucleosynthesis (BBN), but it has been argued that the impact on the primordial deuterium and helium abundances is within observational uncertainties (section 3.1.2 of HBK20).

Structure formation is faster in ν HDM due to the MOND gravity law (Katz et al. 2013). This can better account for the high redshift, mass, and collision velocity of the interacting galaxy clusters known as El Gordo (Menanteau et al. 2010, 2012), which are incompatible with Λ CDM at $> 5\sigma$ confidence for any plausible collision velocity (Asencio, Banik & Kroupa 2021, 2023). The enhanced structure formation on large scales also makes it easier to form the KBC supervoid (Keenan, Barger & Cowie 2013), an extended underdensity that appears to be $46 \pm 6\%$ less dense than the cosmic mean out to 300 Mpc based on the near-infrared galaxy luminosity density in redshift space. The actual underdensity is probably around half that, but even so, the KBC void contradicts Λ CDM at 6σ confidence (section 2 of HBK20). Those authors estimated in their section 1.1 that if the KBC void gradually deepened with time to its presently observed underdensity, then outflows from the KBC void would cause the apparent local expansion rate to exceed the background $H_0 \equiv \dot{a}$ by about 11%, where $H \equiv \dot{a}/a$ is the Hubble parameter at some epoch, a is the cosmic scale factor normalised to unity today, overdots denote time derivatives, and 0 subscripts denote present values, so for instance H_0 is the present expansion rate or Hubble constant.¹

Remarkably, there is strong observational evidence for just such a mismatch in terms of the Hubble tension, the observation that the locally estimated H_0 is about 10% higher than predicted in Λ CDM with parameters calibrated to the CMB power spectrum (Riess & Breuval 2024; Uddin et al. 2024; Bhardwaj et al. 2025; Freedman et al. 2025; Jensen et al. 2025; Said et al. 2025; Scolnic et al. 2025; Vogl et al. 2025). Observers estimate H_0 locally by measuring the distances and redshifts to nearby objects such as galaxies and supernovae (SNe), with the results plotted on a Hubble diagram. The redshift rises almost linearly with the distance r . If we assume that the redshift arises entirely from cosmic expansion, then this linear relation or Hubble law is caused by the fact that photons from an object at distance r were emitted in the past, with the universe having expanded in the meantime. We can then apply the chain rule to get that $H_0 = cz'$, where primes indicate a radial derivative and c is the speed of light (Mazurenko, Banik & Kroupa 2025).

¹ It is constant in space, but not over time.

HBK20 used semi-analytic models to consider the formation of the KBC void out of a small initial density fluctuation at $z = 9$. They found that outflow from the KBC void could quite plausibly inflate the local cz' enough to solve the Hubble tension while having a lower \dot{a} consistent with the CMB observations and other constraints like the ages of the oldest stars (Banik & Samaras 2025, and references therein). This self-consistent void outflow solution to the Hubble tension was later shown to provide a good match to baryon acoustic oscillation (BAO) measurements over the last twenty years (Banik & Kalaitzidis 2025) and the observed bulk flow curve, a measure of the peculiar velocity field in the local Universe (Mazurenko et al. 2024). The observed bulk flow is around quadruple the Λ CDM expectation on the largest probed scale of $250/h$ Mpc, where h is the Hubble constant in units of 100 km/s/Mpc (Watkins et al. 2023). This leads to $> 5\sigma$ tension with Λ CDM expectations, as shown in their figure 8. In short, ν HDM seems to better account for El Gordo, the KBC void, and the fast observed bulk flows at $z \lesssim 0.1$, all of which are severely problematic for Λ CDM while being based on quite different observational techniques.

However, hydrodynamical cosmological ν HDM simulations indicate that galaxies only form by $z \approx 4$ (Wittenburg et al. 2023), in strong disagreement with observations by the *James Webb Space Telescope* (JWST) of galaxies already at $z = 14$ (Carniani et al. 2024). The stronger MOND gravity at $z \lesssim 50$ (section 3.1.3 of HBK20) struggles to compensate for the lack of CDM, which severely reduces the density perturbations on galaxy scales at early times (see figure 1 of Wittenburg et al. 2023). These difficulties with both paradigms suggest that both may have desirable features that should be preserved in a more complete theory. In particular, ν HDM simulations can give insight into what phenomena to expect if structure formation is more rapid than expected in Λ CDM, as suggested by some observations (see also Migkas et al. 2021; Lopez et al. 2022, 2024, though see Sawala et al. 2025).

In this contribution, we explore the ν HDM paradigm using large collisionless simulations on Gpc scales. After covering the governing equations, we explain how we obtain the initial conditions for our ν HDM simulations and how we advance them (Section 2). We then describe our analyses of the resulting particle phase space information (Section 3). We present the results of these analyses in Section 4 and discuss our findings in Section 5. We conclude in Section 6.

2 THEORY AND METHODS

The general methodology we follow is similar to that of Wittenburg et al. (2023), whose main points we briefly recap below.

2.1 Governing equations

Equation 1 is only a heuristic argument for how g_N should be modified in order to explain galaxy rotation curves. It specifies only the asymptotic limits, but we can generalise it to arbitrary g_N by writing that for an isolated spherically symmetric system,

$$g = g_N \nu(g_N), \quad (2)$$

where the interpolating function ν takes argument g_N . In this contribution, we will use the simple interpolating function (Famaey & Binney 2005):

$$\nu = \frac{1}{2} + \sqrt{\frac{1}{4} + \frac{a_0}{g_N}}. \quad (3)$$

Gravity law	Dominant matter component	
	CDM	HDM
Newton	Λ CDM	Λ HDM
MOND	ν CDM	ν HDM

Table 1. Summary of the models considered in this contribution.

This introduces a fairly gradual transition between the Newtonian and deep-MOND regimes, providing a much better fit to the observations (see figure 23 of Banik et al. 2024). In particular, this simple form is numerically quite similar to the exponential form advocated by McGaugh, Lelli & Schombert (2016) based on the Spitzer Photometry and Accurate Rotation Curves (SPARC; Lelli et al. 2016) catalogue of galaxy rotation curves and near-infrared photometry:

$$\nu \left(\frac{g_N}{a_0} \right) = \frac{1}{1 - \exp \left(-\sqrt{\frac{g_N}{a_0}} \right)}. \quad (4)$$

Since we focus on large-scale structure in this contribution, our results are sensitive mainly to the low-acceleration limit in which $g \rightarrow \sqrt{g_N a_0}$ and thus $\nu \rightarrow \sqrt{a_0/g_N}$. The above exponential suppression of the MOND corrections to g_N in the Newtonian regime causes some difficulties in numerical simulations, so we opt to use Equation 2, which has previously been shown to give excellent numerical performance when solved on a grid to obtain the MOND gravitational field (see figure 1 of Banik & Zhao 2018).

In the quasilinear formulation of MOND (QUMOND; Milgrom 2010), more complicated geometries are handled by taking the divergence of both sides in Equation 2:

$$\nabla \cdot \mathbf{g} = \nabla \cdot (\nu \mathbf{g}_N). \quad (5)$$

This introduces an innovative two-step procedure in which we first have to find \mathbf{g}_N using standard techniques based on the input density distribution, find ν using basic algebra and thereby obtain the source term for \mathbf{g} , and repeat the first step using $\nabla \cdot (\nu \mathbf{g}_N)$ as the density field. Only the ordinary Poisson equation has to be solved, allowing the use of standard numerical techniques, albeit applied twice. In a cosmological context, \mathbf{g}_N is sourced only by the density less the cosmic mean density at that epoch (Sanders 2001; Nusser 2002). It has been argued that this Jeans swindle-like (Jeans 1902) approach is valid in some relativistic theories of MOND (Thomas, Mozaffari & Zlosnik 2023), but this is not necessarily guaranteed.

2.2 Models

In addition to the ν HDM model, we perform a benchmark Λ CDM simulation for comparison purposes. We also consider two intermediary models we dub Λ HDM and ν CDM, which consist of Newtonian gravity with HDM initial conditions and MOND gravity with CDM initial conditions, respectively (ν in this context is better thought of as representing the MOND interpolating function in Equation 2 rather than sterile neutrinos). We include these simulations as a reference to better understand the differences between each model, since directly comparing Λ CDM to ν HDM makes it difficult to distinguish whether any differences in behaviour are due to a lack of CDM or due to the MOND gravity law. The different types of model we consider are summarized in Table 1. We note that although one can envisage other approaches to MOND on cosmological scales with the same limiting behaviour in galaxies, a lack of CDM is a generic prediction of any MOND cosmology.

2.3 Initial conditions

The initial conditions for our simulations were generated using the Code for Anisotropies in the Microwave Background (CAMB; Lewis, Challinor & Lasenby 2000) and Multi Scale Initial Conditions for cosmological simulations (MUSIC; Hahn & Abel 2011). A basic overview of the process is that CAMB generates a power spectrum $P(k)$, which MUSIC then samples to produce the initial positions and velocities of the simulation particles. Whilst MUSIC does have an inbuilt functionality to produce its own spatial matter power spectrum, CAMB was used instead due to its increased flexibility with user defined cosmological parameters.

The first step is to select the cosmological parameters that should be used by CAMB. Since an explicit assumption of our cosmological MOND models is that the standard Λ CDM interpretation of the CMB temperature anisotropies is correct, we set most of our cosmological parameters equal to the values found by Planck Collaboration VI 2020 (see the sixth column of their table 2). We therefore adopt the following parameters: $\Omega_m = 0.314595$, $\Omega_b = 0.049271$, $\Omega_\Lambda = 0.685405$, $\sigma_8 = 0.8101$, $n_s = 0.9660499$, and $H_0 = 67.4 \text{ km s}^{-1} \text{ Mpc}^{-1}$ ($h = 0.674$). The density parameters for CDM and neutrinos (Ω_c and Ω_ν , respectively) depend on the model as follows:

$$\Omega_c = \begin{cases} 0.264157 & (\text{CDM}), \\ 0 & (\text{HDM}) \end{cases} \quad (6)$$

and

$$\Omega_\nu = \begin{cases} 0.001167 & (\text{CDM}), \\ 0.265324 & (\text{HDM}). \end{cases} \quad (7)$$

In the HDM simulations, we remove the CDM component and fill up the remaining matter budget with an extra species of sterile neutrino. These can be incorporated into CAMB by modifying the ‘ini’ file (as laid out by Angus 2009; Wittenburg et al. 2023) to include the following parameters:

```
massless_neutrinos = 2.0293
nu_mass_eigenstates = 2
massive_neutrinos = 1 1
nu_mass_degeneracies = 1.0147 1
nu_mass_fractions = 0.0044 0.9956.
```

This ensures that the properties of the active neutrinos are unchanged, whilst also adding in our sterile neutrino component. There is no explicit input for the sterile neutrino mass here. Instead, CAMB assumes the neutrinos are thermalised at recombination, which then leads to a self-consistent calculation of the particle mass, this being $\approx 11 \text{ eV}/c^2$ for this choice of parameters. A limitation here is that CAMB is not designed to implement heavier sterile neutrino masses as they will not be thermal in origin (i.e., their relic abundance would not match the active neutrino relic abundance at recombination). An analytic cut-off to the CDM power spectrum (such as that described by Abazajian 2006) would suffice if heavier sterile neutrinos were desired, but we want the total mass density to remain the same, requiring a lower number density. Results in this case would presumably be intermediate between our MOND simulations with CDM and HDM, i.e., our ν CDM and ν HDM models, respectively (Table 1).

The next step is to define an initial power spectrum $P_i(k)$ and evolve the corresponding initial density perturbations to the starting

simulation redshift of 199 ($a = 0.005$). To do this, the `CAMB` code assumes there was an early inflationary period which produces a “nearly scale-invariant” power spectrum (Harrison 1970; Zeldovich 1972). This is described by

$$P_i(k) \propto k^{n_s-1}, \quad (8)$$

where k is the comoving wavenumber and n_s is the tilt of the scalar spectral index. The overall amplitude is determined by σ_8 . The initial density perturbations are related to the power spectrum by

$$P(k) \propto \delta^2(k). \quad (9)$$

A transfer function $T(k)$ can be calculated to relate these perturbations to those at a later redshift (Eisenstein & Hu 1998). For comparing some early redshift z_a with a later redshift z_b , $T(k)$ would be defined as

$$T(k) \equiv \frac{\delta(z_b, k)}{\delta(z_a, k)}, \quad (10)$$

which can be computed numerically using linear perturbation theory. One caveat is that density perturbations at both z_a and z_b must still be in the linear regime, which will limit the starting redshift of the simulation.

From Equations 9 and 10, we can see that $P(k)$ and $T(k)$ can be directly related by

$$P_b(k) = P_a(k) T^2(k), \quad (11)$$

where we use a and b subscripts to denote the two redshifts we are considering. Therefore, once the transfer function has been calculated by `CAMB`, it is used to calculate the power spectrum at the starting redshift of the simulation for use by `MUSIC`.

For these simulations, the early redshift z_a would occur just after the end of the inflationary period and be determined by `CAMB`, while z_b would correspond to when we start our simulations. We select the starting redshift as $z_i = 199$. This is late enough that the radiation component of the universe (which will not be simulated) has a negligible density, whilst also early enough that the MOND effects are suppressed. This second point is justified by the work of Haslbauer et al. (2020), who find that density perturbations do not enter the MOND regime until $z \lesssim 50$. We will further corroborate this prediction in Section 4.1.

In CDM models, the transfer function is always positive at epochs much later than recombination because the CDM coalesces in the initial overdensities, thereby preserving them during the oscillations of the baryon-photon fluid. The same logic applies to underdensities. Initial overdensities do not turn into underdensities, and vice versa. Baryons do of course undergo oscillations (Section 1), but they subsequently fall into the much deeper potential wells generated by the CDM, so the initial density perturbation has the same sign as the density perturbation subsequent to recombination after a very short delay. However, since HDM will free-stream out of small-scale overdensities, oscillations of the baryon-photon fluid can erase these overdensities. This can lead to a negative transfer function, representing scales where initially overdense regions have become underdense by $z = 199$, and vice versa (Wittenburg et al. 2023). This is not problematic theoretically, since Equation 11 shows that the phase of the transfer function is unimportant for the power spectrum. Logistically though, this process requires us to make a slight modification to the `MUSIC` code to read in the magnitude of the transfer function. This is because the logarithm of the transfer function is used, so the value must be positive.

Once $T(k)$ has been read in, `MUSIC` will generate initial particle positions and velocities by convolving $T(k)$ with random Gaussian

white noise (Hahn & Abel 2011). All simulations presented here were generated using the same random seed. Some further parameters provided in the `MUSIC` “.conf” file are:

```
boxlength = 800
zstart = 199
levelmin = 8
levelmax = 10
baryons = no
periodic_TF = yes.
```

This will generate a box with sides of $800/h$ comoving Mpc (cMpc) at a starting redshift of $z_i = 199$, which is set by the “zstart” parameter. The “baryons = no” option sets the simulation to assume all the matter is collisionless, which should be an appropriate approximation on the scales we investigate. “levelmin” defines the base coarse grid for the box and also the number of simulation particles, which is $N_{\text{part}} = 2^{3 \text{levelmin}}$. Hence these simulations have 256^3 particles and a mass per particle of $2.67 \times 10^{12} h^{-1} M_{\odot}$. The maximum spatial resolution is defined by “levelmax” and will be $781/h$ ckpc in this case. The “periodic_TF” option gives the simulation periodic boundary conditions.

The authors of Wittenburg et al. (2023) made some slight adjustments to the output files of `MUSIC` so that they are compatible with the simulation code used. The modified version of `MUSIC` used here is publicly available.²

2.4 Simulation code

The simulations were performed using `PHANTOM OF RAMSES` (POR; Lüghausen, Famaey & Kroupa 2015), a modified version of the Adaptive Mesh Refinement (AMR) code `RAMSES` (Teyssier 2002). We used the collisionless N -body mode, which enables only gravitational interactions and treats all particles as point-like. MOND is integrated into the `POR` code by solving the ordinary Poisson equation twice, once to obtain \mathbf{g}_N and another time to solve Equation 5, with a simple algebraic calculation and numerical differentiation in between.

The authors of Wittenburg et al. (2023) made further modifications to this code so that it can be applied to cosmological simulations, in particular by using supercomoving coordinates (Martel & Shapiro 1998; Teyssier 2002). Comoving coordinates provide a more natural coordinate system to incorporate the expansion of the universe, but it is also convenient to apply several other scalings inspired by similar modifications made to the `RAYMOND` code (Candlish et al. 2015; Candlish 2016). For instance, comoving positions are divided by the comoving box size, the comoving density is divided by the average for the simulation box, and times are in units of the present Hubble time $1/H_0$ (see appendix A of Wittenburg et al. 2023). More details on the specifics of these overall modifications are provided in Wittenburg et al. (2020) and Wittenburg et al. (2023), while Nagesh et al. (2021) provides a user guide for `POR`.

² https://bitbucket.org/SrikanthTN/bonmpor/src/master/Cosmo_patch_and_setup_and_halofinder/music/

3 ANALYSIS OF SIMULATION OUTPUTS

We use the `EXTRACT_POR` tool to extract the individual particle data from the binary simulation outputs and represent them in ASCII form.³ The front bottom left corner of the simulated domain is at the origin, so the x , y , and z coordinates are all ≥ 0 .

Due to computational and time constraints, locally inferred parameters were measured from a subset of 25^3 particles, which we call ‘‘vantage points’’ (VPs). We run analyses at different VPs in parallel, with the computational efficiency further improved by using a basic tree code in which particles are sorted into 100^3 voxels (this is similar to the approach used in [Banik et al. 2021](#), whose tree code implementation is publicly available). The VPs are chosen by splitting the simulation volume into 25^3 voxels and then searching for the particle closest to the centre of each voxel. We require the VP particle to be within $16/h$ Mpc of the voxel centre to limit the overlap between any two VPs, which is another reason not to consider a too dense grid of VPs. Considering results from a simulation particle should provide a fair representation of the simulation as a whole, without overly biasing them to, e.g., overdense regions where more particles are present. Requiring each VP to reside at a particle should also provide a fairer comparison to what a real observer could see – it would be very difficult for us to measure anything from a region with no galaxies to live in!

Once we have selected the VPs from which to do our analyses, we then calculate the locally inferred density contrast, bulk flow, apparent Hubble constant and deceleration parameter, and Hubble dipole that an observer would measure from the VP. We detail the methodology for these calculations below in Sections 3.2, 3.3, 3.4, and 3.5, respectively. We also apply a group-finding algorithm to identify haloes that are likely gravitationally bound (Section 3.1).

3.1 Halo counts

A simple way to quantify structure formation is with the Cumulative Halo Mass Function (CHMF), the comoving number density of haloes above some specified mass. This $n(M)$ has been determined observationally by studies such as [Driver et al. \(2022\)](#) and [Wang et al. \(2022\)](#) using the Galaxy and Mass Assembly (GAMA; [Driver et al. 2009](#)) survey and the Dark Energy Spectroscopic Instrument (DESI) Legacy Imaging Survey DR9 ([Dey et al. 2019](#)), respectively.

We choose [Driver et al. \(2022\)](#) as the observational reference because they probe to higher masses, better complementing our large-scale simulations. Their method fits the observed halo mass function to the ‘MRP function’ given by [Murray, Robotham & Power \(2018\)](#):

$$\begin{aligned} \phi[\log_{10}(M/M_{\odot})] &\equiv \frac{dn}{d(\log_{10}(M/M_{\odot}))} \\ &= \ln(10)\phi_*\beta\left(\frac{M}{M_*}\right)^{\alpha+1} \exp\left[-\left(\frac{M}{M_*}\right)^{\beta}\right]. \end{aligned} \quad (12)$$

We use their ‘Omega’ parameter fit (which enforces the [Planck Collaboration VI 2020](#) Ω_m as a prior) and correct to $z = 0$ such that $\log_{10}\phi_* = -4.565^{+0.29}_{-0.24}$ Mpc⁻³ dex⁻¹, $\log_{10}(M_*/M_{\odot}) = 14.505^{+0.11}_{-0.15}$, $\alpha = -1.85^{+0.03}_{-0.03}$, and $\beta = 0.77^{+0.11}_{-0.11}$. The CHMF is

then found by integrating [Equation 12](#) in log-space to $+\infty$ such that

$$N(>M) = \int_M^{+\infty} \phi[\log_{10}M'] d(\log_{10}M'). \quad (13)$$

This observed CHMF is stated to be valid in the range $10^{12.5}M_{\odot}/h < M < 10^{15.3}M_{\odot}/h$.

To identify haloes in the simulations, we use the HOP ([Eisenstein & Hut 1998](#)) group-finding algorithm built into the `YT_ASTRO_ANALYSIS` extension ([Smith et al. 2022](#)) of the `YT` analysis toolkit ([Turk et al. 2011](#)). This is a density-based group-finding algorithm which links particles to a group using their highest density neighbour. The local density at each particle is calculated by the radial distance to the closest N_{dens} particles. We use a base value of $N_{\text{dens}} = 65$. Particles are linked into ‘‘chains’’ using their highest density neighbour, until a particle is reached that has a higher density than all of its neighbours. A group about this particle is formed from all the chains that connect to it. These groups are then accepted or rejected based on an arbitrary density threshold, which we take to be an overdensity of $200\times$ the critical density ρ_c to match [Driver et al. \(2022\)](#). The algorithm therefore outputs a mass of M_{200} and corresponding virial radius of R_{200} , which are related by

$$M_{200} \equiv (200\rho_c)\left(\frac{4\pi R_{200}^3}{3}\right). \quad (14)$$

A few other useful quantities are also extracted.

As discussed by [Wittenburg et al. \(2023\)](#), algorithms such as HOP are built for simulations using Newtonian gravity, with no equivalent algorithms yet made for MOND gravity. We follow their example and report a Newtonian dynamical mass M_N for the structures identified.

$$M_N = \nu\left(\frac{g_N}{a_0}\right)M_{200}, \quad (15)$$

where g_N is evaluated at the virial radius M_{200} , giving

$$g_N = \frac{GM_{200}}{R_{200}^2}. \quad (16)$$

This modification was inspired by a similar technique used by [Angus et al. \(2011\)](#). It allows for a fairer comparison between the MOND simulations and observations. All halo masses presented for the MOND simulations will be these Newtonian dynamical masses, which better correspond to the mass that observers would report in the literature using probes of the internal dynamics or lensing.

This general boost to the gravity caused by MOND likely also means that there are bound structures which are overlooked by the HOP algorithm, which a specialised MOND groupfinder would detect. The number counts reported by HOP may therefore be better interpreted as a lower bound on the true number counts for the MOND simulations.

Previous work has suggested that simulations with warm DM (WDM) or HDM may produce spurious small-scale structures ([Colín et al. 2008](#); [Power et al. 2016](#)). To curb the effect of any such small-scale issues, we conservatively require all considered haloes to have ≥ 100 particles.

Once the haloes have been identified, the simulated CHMF can be calculated by dividing the number of haloes above a given mass by the comoving simulation volume. The results are shown in [Section 4.2](#).

³ https://bitbucket.org/SrikanthTN/bonnpor/src/master/extract_por/

3.2 Density contrast

The simplest location-dependent parameter is the average density in some suitably chosen volume centred on each VP. Since we also know the average density $\bar{\rho}$ in our simulation box from the adopted cosmological parameters or analysis of the results, the first locally inferred parameter we measure is the fractional density contrast δ . In order to better replicate the observations taken by Keenan, Barger & Cowie (2013) and Wong et al. (2022), we only consider particles within $R_\delta = 225/h$ Mpc and beyond $r_\delta = 27/h$ Mpc of each VP, ignoring particles outside this distance range. This is to replicate the redshift range of Wong et al. (2022). We also mask a randomly oriented region of the sky at each VP to mimic the obscuring effect of the Galactic disc. We follow the procedure laid out by HBK20, which we briefly revisit.

We begin by setting the visible area A of the sky equal to the survey area, which in our case is $A = 37080 \text{ deg}^2$ as stated in section 2.5 of Keenan, Barger & Cowie (2013).⁴ The direction of the masked region is randomly chosen for each VP based on a random direction, which is analogous to the north Galactic pole. For this, we sample two random numbers u_θ and u_ϕ that are uniform over the range $0 - 1$, i.e., $u_\theta, u_\phi \sim \mathcal{U}(0, 1)$. We then calculate the polar angle θ and azimuthal angle ϕ as follows:

$$\cos \theta = 2u_\theta - 1, \quad (17)$$

$$\phi = \cos(2\pi u_\phi). \quad (18)$$

The corresponding unit vector $\hat{\mathbf{n}}$ representing the Galactic spin axis is then

$$\hat{\mathbf{n}} \equiv \begin{pmatrix} \hat{\mathbf{n}}_x \\ \hat{\mathbf{n}}_y \\ \hat{\mathbf{n}}_z \end{pmatrix} = \begin{pmatrix} \sin \theta \cos \phi \\ \sin \theta \sin \phi \\ \cos \theta \end{pmatrix}. \quad (19)$$

Since the Galactic disc is positioned in the plane perpendicular to $\hat{\mathbf{n}}$, observers see galaxies only close to $\pm\hat{\mathbf{n}}$. The angular radius of the masked region near the Galactic equator can be calculated by relating the surface area element and solid angle element of a unit sphere. This relation can be expressed as the following integral:

$$A = 2 \int_0^{2\pi} \int_0^{\frac{\pi}{2} - \omega_\delta} \sin \theta \, d\theta \, d\phi, \quad (20)$$

where ω_δ is the half-angle width of the sky region obscured by the Galactic disc, or equivalently the minimum observable Galactic latitude. Evaluating this integral and rearranging gives

$$\cos \omega_\delta = 1 - \frac{A}{4\pi}, \quad (21)$$

which matches equation 14 of HBK20.

A particle p is accepted into the analysis if its position \mathbf{r}_p relative to the VP is within $\frac{\pi}{2} - \omega_\delta$ of the axis defined by $\pm\hat{\mathbf{n}}$, taking the sign that gives the smaller angle. This can be expressed mathematically through the dot product as follows:

$$|\mathbf{r}_p \cdot \hat{\mathbf{n}}| > r_p \cos \omega_\delta, \quad (22)$$

where $r \equiv |\mathbf{r}|$ for any vector \mathbf{r} in what follows, so in this case r_p is the distance of particle p from the observer. The modulus is required on the left hand side because valid positions unobscured by the mock Galactic disc are found both above and below it. Any particle that does not meet this condition is masked by the mock Galactic disc and ignored.

⁴ This is very similar to the 37063 deg² stated in table 1 of Wong et al. (2022).

We find the total mass M of all particles within R_δ and beyond r_δ that are unobscured by the mock Galactic disc. The volume of the considered region is thus

$$V = \frac{2\pi (R_\delta^3 - r_\delta^3)}{3} (1 + \cos \omega_\delta). \quad (23)$$

The locally inferred density contrast is then

$$\delta \equiv \frac{M}{V\bar{\rho}} - 1. \quad (24)$$

We show our simulated density contrasts in Section 4.3.

3.3 Bulk flows

The final particle level analysis we perform is calculating bulk flows so that they can be compared to Watkins et al. (2023). We mimic their approach and draw a sphere around each VP, split into equally spaced radial bins of width $25/h$ Mpc. The innermost bin of each sphere extends up to $r_{\text{bf,in}} = 25/h$ Mpc and the outermost bin extends up to $r_{\text{bf,out}} = 400/h$ Mpc, for a total of 16 bins. Measuring out to such large radii also allows us to check the possibility of a bulk flow sourcing the Hubble dipole observed by Migkas et al. (2021).

To create an equivalent comparison to Watkins et al. (2023), we calculate bulk flows using only the line of sight (LOS) or radial peculiar velocity $v_{r,p}$ of particle p from each VP (Equation 30). This requires us to first calculate the unit vector $\hat{\mathbf{n}}_p$ of particle p from the VP.

$$\hat{\mathbf{n}}_p \equiv \frac{\mathbf{r}_p}{r_p}. \quad (25)$$

Although $v_{r,p}$ is usually considered a scalar quantity, we will interpret it as a vector by assigning it the LOS direction.

$$\mathbf{v}_{r,p} = v_{r,p} \hat{\mathbf{n}}_p. \quad (26)$$

The bulk flow at radius R can then be calculated as

$$\mathbf{v}_{\text{bf}}(R) = \frac{3 \sum_{p(<R)} \left(\frac{M_p \mathbf{v}_{r,p}}{r_p^2} \right)}{\sum_{p(<R)} \left(\frac{M_p}{r_p^2} \right)}, \quad (27)$$

where $\sum_{p(<R)}$ represents a sum over all particles within radius R . The factor of 3 here comes from equation 2 of Nusser (2016). It ensures that if all particles within the considered volume had the same \mathbf{v} , then the inferred bulk flow would be $\mathbf{v}_{\text{bf}} = \mathbf{v}$. The projection of \mathbf{v} onto the LOS and the projection of the LOS onto the direction of \mathbf{v} result in an average factor of 1/3 (Mazurenko et al. 2024). This is cancelled out by introducing an extra factor of 3 into the definition of the bulk flow. Therefore, we can approximately equate \mathbf{v}_{bf} with the mass-weighted mean velocity of all the matter within R , even though strictly speaking this requires knowledge of 3D velocities and thus cannot be obtained by observers using only LOS peculiar velocities. A major advantage of using bulk flows rather than peculiar velocities is that the latter can only be obtained from the independent observables of redshift and distance if we know H_0 , which however is highly controversial. But since the bulk flow is an average velocity within a spherical region, it is insensitive to the assumed value of H_0 . This is because roughly speaking, it measures the dipole angular variation in redshift at fixed distance.

Our simulated bulk flows are shown in Section 4.4, with a comparison to the reported angle between the observed Hubble dipole and local bulk flow found in Section 4.6.

3.4 Hubble constant and deceleration parameter

The background Hubble constant in our simulations is $H_0 = 67.4$ km/s and the background deceleration parameter is

$$q_0 \equiv -\frac{\ddot{a}a}{\dot{a}^2} = \frac{\Omega_m}{2} - \Omega_\Lambda = 0.53. \quad (28)$$

However, systematic effects due to large-scale structure, such as outflows from a local supervoid, may offset an observers' measurement of these parameters from their true values (Section 1.2). In what follows, we use \mathbf{v} to denote a peculiar velocity. Following the procedure of [HBK20](#), we construct a quadratic model for v_r , the radially outward component of \mathbf{v} from a particular VP. We calculate results at thousands of different VPs to explore what the universe would look like from different viewpoints.

Since we have a large number of particles, we obtain the mean v_r in shells, yielding a curve of $\bar{v}_r(r)$, where r is the distance from the observer. We begin by constructing a hollow sphere with inner radius $r_{H,in} = 70/h$ Mpc ($z \approx 0.023$) and outer radius $r_{H,out} = 400/h$ Mpc ($z \approx 0.14$) around each VP, comparable to the redshift range used in [Camarena & Marra 2020](#) ($0.023 < z < 0.15$), with whom we compare. Since our simulations have a box length of $800/h$ Mpc, we cannot further extend the outer radius in this analysis without double-counting particles. We split each hollow sphere into ten equally spaced radial bins of width $33/h$ Mpc. For any given bin b , we define its mass-weighted distance from the observer as

$$\bar{r}_b \equiv \frac{\sum_p M_p r_p}{\sum_p M_p}, \quad (29)$$

where an overline denotes a mass-weighted average, p is the index of each particle with position vector \mathbf{r}_p relative to the VP, and \sum_p is a sum over all particles in bin b . Similarly, we find the mass-weighted v_r as follows:

$$\bar{v}_b \equiv \frac{\sum_p M_p \overbrace{(\mathbf{r}_p \cdot \mathbf{v}_p / r_p)}^{v_{r,p}}}{\sum_p M_p}, \quad (30)$$

omitting the r subscript on \bar{v} for clarity and using \mathbf{v}_p for the peculiar velocity vector of particle p . Peculiar velocities in the simulation frame are first corrected for the overall barycentre peculiar velocity and therefore correspond to observed velocities in the CMB frame, which is the usual convention because the velocity of the Sun relative to the CMB is known very precisely ([Smoot et al. 1977](#); [Kogut et al. 1993](#)). Observers therefore typically convert velocities in the less fundamental heliocentric frame to the more fundamental CMB frame (see also [Wagenveld et al. 2024](#)).

We now fit the binned outward peculiar velocity \bar{v}_r using a parabolic dependence on \bar{r} :

$$\bar{v}_b(\bar{r}) = \mathcal{A}_H \bar{r}_b^2 + \mathcal{B}_H \bar{r}_b, \quad (31)$$

where \mathcal{A}_H and \mathcal{B}_H are free parameters to be fit for each VP, allowing us to gauge the relation with other observer-dependent quantities like the local density contrast (Section 3.2). Our approach is different from standard polynomial fitting because we force the intercept to be zero. This is because physically the outward velocity at zero distance from any observer must be zero to have a continuous velocity field. To find the best-fitting coefficients \mathcal{A}_H and \mathcal{B}_H , we construct a quadratic loss function λ as follows:

$$\lambda\{\bar{r}_b, \bar{v}_b\} = \sum_b \left[\bar{v}_b - \left(\mathcal{A}_H \bar{r}_b^2 + \mathcal{B}_H \bar{r}_b \right) \right]^2, \quad (32)$$

where \sum_b is a sum over all bins. The optimal solution for \mathcal{A}_H and \mathcal{B}_H is found when λ is minimised, requiring that $\frac{\partial \lambda}{\partial \mathcal{A}_H} = 0$ and $\frac{\partial \lambda}{\partial \mathcal{B}_H} = 0$. Calculating these partial derivatives produces the following simultaneous equations:

$$\begin{aligned} \sum_b \bar{r}_b \bar{v}_b &= \mathcal{A}_H \sum_b \bar{r}_b^3 + \mathcal{B}_H \sum_b \bar{r}_b^2 \\ \sum_b \bar{r}_b^2 \bar{v}_b &= \mathcal{A}_H \sum_b \bar{r}_b^4 + \mathcal{B}_H \sum_b \bar{r}_b^3. \end{aligned}$$

We use Gaussian elimination to solve these simultaneous equations for \mathcal{A}_H and \mathcal{B}_H .

We next use these coefficients to estimate \mathcal{H}_0 and \mathcal{Q}_0 , the apparent Hubble and deceleration parameters deduced assuming only cosmological expansion contributes to the redshift. In reality, the wavelength of a photon gets stretched both due to cosmological expansion and outward peculiar velocity v_r , so the redshift z satisfies

$$(1+z) = (1+z_c)(1+v_r/c), \quad (33)$$

where $z_c \equiv a^{-1} - 1$ is the purely cosmological contribution to z . We can invert this relation to find the apparent cosmic scale factor a_{app} that would be found if redshifts were assumed to arise solely from cosmic expansion:

$$a_{\text{app}} = \frac{1}{1+z} = \frac{a}{1+v_r/c}. \quad (34)$$

Differentiating with respect to time gives

$$\dot{a}_{\text{app}} = \frac{\dot{a}}{1+v_r/c} - \frac{a}{c(1+v_r/c)^2} \dot{v}_r \quad (35)$$

$$= \frac{\dot{a}}{1+v_r/c} + \frac{a}{(1+v_r/c)^2} v'_r, \quad (36)$$

where we used the relation $dr = -c dt$ for our past lightcone, approximating that v_r has changed little in the light crossing time of any local inhomogeneity. At $a = 1$ and $v_r = 0$, we get that

$$\mathcal{H}_0 \equiv \dot{a}_{\text{app}} = \dot{a} + v'_r = \dot{a} + \mathcal{B}_H, \quad (37)$$

substituting in our parabolic binned relation between v_r and r ([Equation 31](#)). We get the expected result that the linear coefficient \mathcal{B}_H acts as an extra contribution to the apparent Hubble constant.

Differentiating [Equation 36](#) with respect to time gives

$$\begin{aligned} \ddot{a}_{\text{app}} &= \frac{\ddot{a}}{1+v_r/c} - \frac{\dot{a}}{c(1+v_r/c)^2} \dot{v} + \frac{\dot{a}}{(1+v_r/c)^2} v'_r \\ &+ \frac{a}{(1+v_r/c)^2} \dot{v}'_r - \frac{2a}{c(1+v_r/c)^3} v'_r \dot{v}_r \end{aligned} \quad (38)$$

$$\begin{aligned} &= \frac{\ddot{a}}{1+v_r/c} + \frac{2\dot{a}}{(1+v_r/c)^2} v'_r - \frac{ac}{(1+v_r/c)^2} v''_r \\ &+ \frac{2a}{(1+v_r/c)^3} v_r'^2. \end{aligned} \quad (39)$$

At $a = 1$ and $v_r = 0$, this reduces to

$$\ddot{a}_{\text{app}} = \ddot{a} + 2\dot{a}v'_r - cv''_r + 2v_r'^2 \quad (40)$$

$$= \ddot{a} + 2v'_r(\dot{a} + v'_r) - cv''_r \quad (41)$$

$$= \ddot{a} + 2(\mathcal{B}_H \mathcal{H}_0 - \mathcal{A}_H c). \quad (42)$$

We then get the background \ddot{a} from [Equation 28](#) and use an analogous relation to obtain the apparent deceleration parameter:

$$\mathcal{Q}_0 \equiv -\frac{\ddot{a}_{\text{app}}}{\mathcal{H}_0^2}. \quad (43)$$

We present the simulated apparent Hubble constant and deceleration parameters in Section 4.5.

3.5 Hubble dipole

Some studies have reported a dipole-like angular variation in the apparent Hubble constant across the sky (Migkas & Reiprich 2018; Kalbouneh et al. 2023; Hu et al. 2024b,c; Sah et al. 2025). We compare our results with the study of Migkas et al. (2021), who used galaxy cluster scaling relations to obtain distances to galaxy clusters, albeit without any absolute calibration. This prevents their study from directly addressing the Hubble tension, but it does allow for an interesting cosmological test using the percentage variation in \mathcal{H}_0 across the sky. Migkas et al. (2021) report a Hubble dipole of $9.0 \pm 1.7\%$ on scales of about $350/h$ Mpc, which is of a similar magnitude to the Hubble tension. They suggest that this signal could be sourced by peculiar velocities, rather than being a physical difference in expansion rate across the sky. We test this hypothesis by quantifying the observed dipole induced by peculiar velocities around each VP.

We begin by obtaining the position r_p relative to the VP and the radially outward peculiar velocity $v_{r,p}$ (Equation 30) for particle p . Since the cluster scaling relations of Migkas et al. (2021) lack any absolute calibration, we need to work out a dipole in percentage terms rather than in km/s/Mpc. This means we need to know the monopole term, which neglecting the Hubble expansion is given by

$$\mathcal{M}(R) = \frac{\sum_{p(<R)} r_p v_{r,p}}{\sum_{p(<R)} r_p^2}, \quad (44)$$

where $\sum_{p(<R)}$ is the sum over all particles within distance R of the VP. In this case, we set $R = 350/h$ Mpc as this roughly corresponds to the typical distance of the galaxy clusters analysed by Migkas et al. (2021).

The dipole \mathcal{D} in the Hubble parameter has the following components:

$$\mathcal{D}_x(R) = \frac{\sum_{p(<R)} x_p v_{r,p}}{\sum_{p(<R)} x_p^2}, \quad (45)$$

$$\mathcal{D}_y(R) = \frac{\sum_{p(<R)} y_p v_{r,p}}{\sum_{p(<R)} y_p^2}, \quad (46)$$

$$\mathcal{D}_z(R) = \frac{\sum_{p(<R)} z_p v_{r,p}}{\sum_{p(<R)} z_p^2}, \quad (47)$$

where x_p , y_p , and z_p are, respectively, the x , y , and z components of r_p . The total inferred Hubble dipole is then simply

$$\mathcal{D}(R) = \sqrt{\mathcal{D}_x(R)^2 + \mathcal{D}_y(R)^2 + \mathcal{D}_z(R)^2}, \quad (48)$$

with the percentage dipole being

$$\mathcal{D}_\% (R) = \frac{100 \mathcal{D}(R)}{H_0 + \mathcal{M}(R)}. \quad (49)$$

Note that since $\mathcal{D}_\%$ is the percentage variation of the apparent Hubble constant, the denominator must include the background cosmological expansion and not just the monopole term of the peculiar velocity field (Equation 44).

Our simulated Hubble dipoles can be found in Section 4.6, along with a comparison to the reported angle between the observed dipole and bulk flow directions.

4 RESULTS

We begin by showing final ($z = 0$) snapshots of our four cosmological simulations (Table 1) in Figure 1. The top row shows results using GR, while the bottom row shows the mixed MOND + DM counterpart. The left and right columns show results when using CDM or HDM, respectively, for the DM component. We will continue this formatting for figures going forward to help visualise which changes are due to the gravity law and which are due to the initial power spectrum on small scales.

The Λ CDM simulation in the top left panel provides a baseline for comparison with the other models. Much more structure is apparent on small scales in the CDM models, presumably because the HDM models have much less initial power on small scales (see figure 1 of Wittenburg et al. 2023). The gravity law also has a significant impact, with much more structure apparent in the MOND models compared to those which assume GR.

Although ν CDM is unrealistic, it shows a highly structured universe resulting from the combination of both MOND and CDM. At the opposite extreme, the Λ HDM model shows only modest signs of structure, and even then only on large scales, demonstrating the importance of CDM to structure formation if assuming GR. The ν HDM model represents a middle ground, but it still looks drastically different to Λ CDM. As discussed in Section 1.2 and Wittenburg et al. (2023), the lack of CDM delays the formation of galaxies. But on large scales, we expect the main difference to be due to the gravity law. Given the very serious problems faced by Λ CDM on large scales such as the Hubble and bulk flow tensions and the KBC supervoid, we explore the behaviour on large scales further.

4.1 Peculiar velocities

Structure growth is also evident in the peculiar velocities v , which are order several hundred km/s today despite being just a few km/s at recombination, as evidenced by the 10^{-5} level temperature fluctuations in the CMB implying peculiar velocities of order $10^{-5} c$. We therefore explore the evolution of the peculiar velocity field. For this, we show the median particle peculiar velocity as a function of a (Figure 2). Linear perturbation theory in GR tells us that the density contrasts grow as $\delta \propto a$ and $v \propto \sqrt{a}$ in the matter-dominated regime, which applies to the majority of cosmic history. Indeed, the top panels of Figure 2 show that this scaling is accurate until the time when dark energy starts to become important, which we indicate with a dashed vertical line towards the right of each panel. Dark energy slows down the growth of structure due to enhanced Hubble drag.

The MOND models also follow the $v \propto \sqrt{a}$ scaling in the first part of our simulation. This is because the accelerations typically exceed a_0 when $z \gtrsim 50$ (see section 3.1.3 of HBK20). At later times, the typical acceleration falls below a_0 , largely putting density perturbations into the MOND regime. As a result, the growth of structure in each MOND model becomes much more rapid than in its GR counterpart, which we show in the panel immediately above. Even so, the MOND models do show a modest deceleration in structure growth at late times due to dark energy, similarly to the models using GR.

To characterise the peculiar velocity distributions in more detail, we show them at $z = 0$ in Figure 3. We add a vertical black line at the observed Local Group (LG) peculiar velocity of $v_{LG} = 627$ km/s (Kogut et al. 1993). Λ CDM and Λ HDM (two leftmost peaks) produce present peculiar velocities of a few hun-

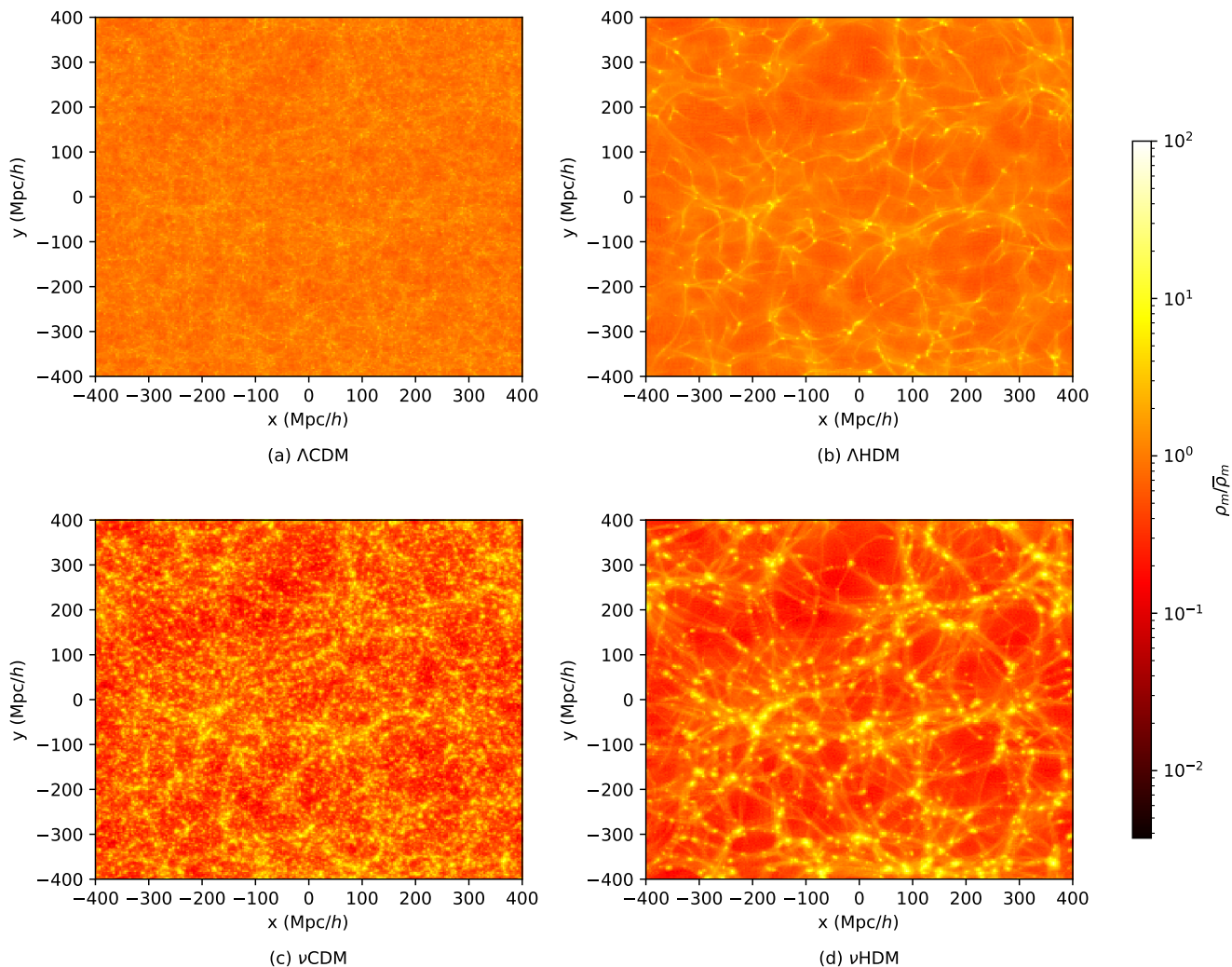


Figure 1. The density projected along the z direction through the whole simulation box at $z = 0$ for Λ CDM (top left), Λ HDM (top right), ν CDM (bottom left), and ν HDM (bottom right). The colour of each pixel shows the average 3D density in the pixel in units of the cosmic mean, as indicated using the logarithmic colour bar. The colour scale is identical for each plot.

dred km/s and can therefore easily account for this observation, but ν CDM and ν HDM (two rightmost peaks) instead yield a few thousand km/s (see also figures 14–16 of Candlish 2016). The peculiar velocities in the MOND models are so large that it is quite unlikely to find ourselves in an environment with as low a peculiar velocity as the LG. In particular, only 30556 (9931) particles have $v \leq v_{\text{LG}}$ in the ν CDM (ν HDM) simulation, which given the total number of particles would make the LG a 2.9σ (3.2σ) outlier. While not conclusive, this is the first indication that ν HDM overcorrects the issues faced by Λ CDM on large scales. In other words, a more accurate description of nature would not enhance the growth of structure as much as ν HDM, though it should do so to a limited extent.

4.2 Cumulative Halo Mass Functions

Our simulations form a large number of gravitationally bound objects by $z = 0$ (as also reported by Wittenburg et al. 2023). We identify these structures using a halo finder (Section 3.1). Due to the larger size of our simulations and their collisionless nature,

these structures correspond to galaxy clusters rather than individual galaxies. We use Figure 4 to show the CHMF, the comoving number density of haloes above some specified mass. The shape of the simulated CHMF is mostly determined by the assumed nature of the DM component, with CDM models giving a more steeply declining CHMF (compare the blue and orange curves with the red and green curves). This is to be expected because CDM is able to cluster much more efficiently on small scales than HDM. The gravity law mostly affects the normalization, with the enhanced gravity law in MOND shifting the CHMF upwards without much altering the shape (compare the blue and orange curves, or the red and green curves).

The solid black points on Figure 4 show the observed CHMF (Driver et al. 2022). This presents a steep decline, which we have seen is characteristic of CDM rather than HDM. The Λ CDM model appears to fit the most massive end of the observations, where a comparison is possible (our simulations lack the resolution at lower mass). None of the other considered models are as successful in this regard. While it is to be expected that HDM cannot account for the observations in the context of GR gravity, both MOND models

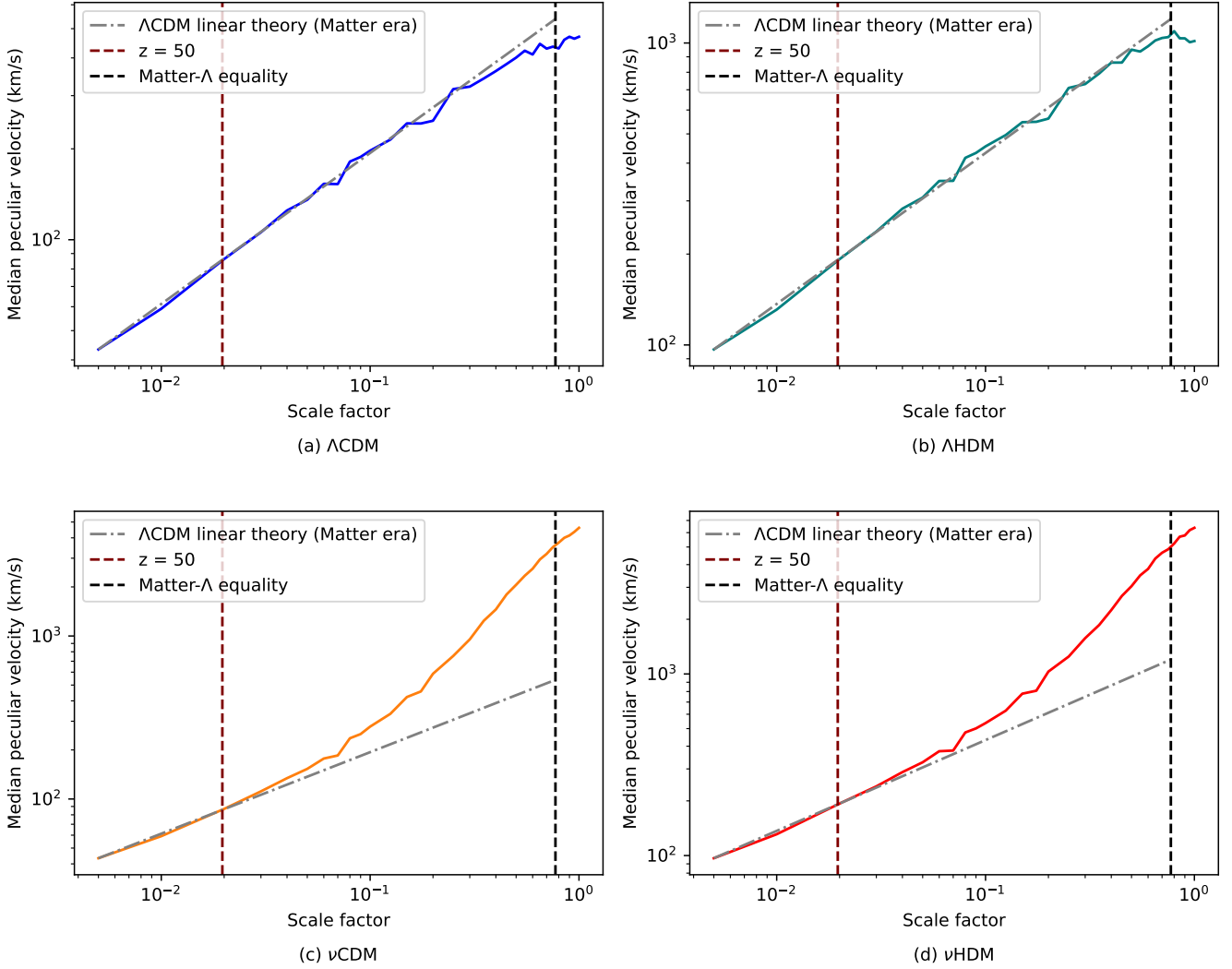


Figure 2. Evolution of the median particle peculiar velocity v with the cosmic scale factor a for Λ CDM (top left), Λ HDM (top right), ν CDM (bottom left), and ν HDM (bottom right). Results are shown on logarithmic axes. The grey dashed-dotted line shows the predicted $v \propto \sqrt{a}$ evolution from linear Newtonian theory in the absence of dark energy, the maroon dashed line shows the $z = 50$ epoch at which overdensities are predicted to enter the MOND regime (HBK20), and the black dashed line shows the epoch of matter-dark energy equality.

are also in severe disagreement with the observations. We confirm with newer observational data the results of earlier simulations by Angus & Diaferio (2011) and Angus et al. (2013), who also found that ν HDM over-predicts the number of massive halos. We iterate upon their results with our ν CDM and Λ HDM simulations to better understand the cause of these issues. In particular, we expect that ν CDM and ν HDM bracket the range of possibilities of similar hybrid MOND + DM models, since DM particles with an intermediate mass (WDM) would presumably give a result intermediate between the two. This highlights a likely problem with such hybrid models: the observed steeply declining CHMF requires significant power on small scales. This is not apparent in the CMB, but we also cannot assign it to the DM component because the DM particles should have a rest energy $\lesssim 300$ eV to avoid destroying the MOND fits to galaxy rotation curves (Angus 2010). Free-streaming effects would then severely limit the power on small scales. One can argue that the power on these scales subsequently grew quite rapidly with MOND gravity. However, this would also cause the power on large scales to grow rapidly, leading to a significant overproduction of the most

massive galaxy clusters. There must inevitably be suppression of power on small scales due to DM free-streaming, but the observations imply that this should occur only on very small scales, below the range of cluster masses probed by Driver et al. (2022). This is a strong argument in favour of CDM particles regardless of the gravity law.

4.3 Local density contrasts

An important constraint on any cosmological model is its ability to reproduce the KBC void, which has an apparent underdensity of $46 \pm 6\%$ out to 300 Mpc (Keenan, Barger & Cowie 2013). Because of redshift space distortions (RSD) due to outflow from the detected void inflating the redshifts, this corresponds to an $\approx 20\%$ underdensity (HBK20). Those authors included an allowance for RSD and compared the observations of Keenan, Barger & Cowie (2013) in redshift space to the Millennium XXL (MXXL) simulation of Λ CDM (Angulo et al. 2012). This comparison shows that Λ CDM fails at 6σ confidence. The results of Keenan, Barger & Cowie

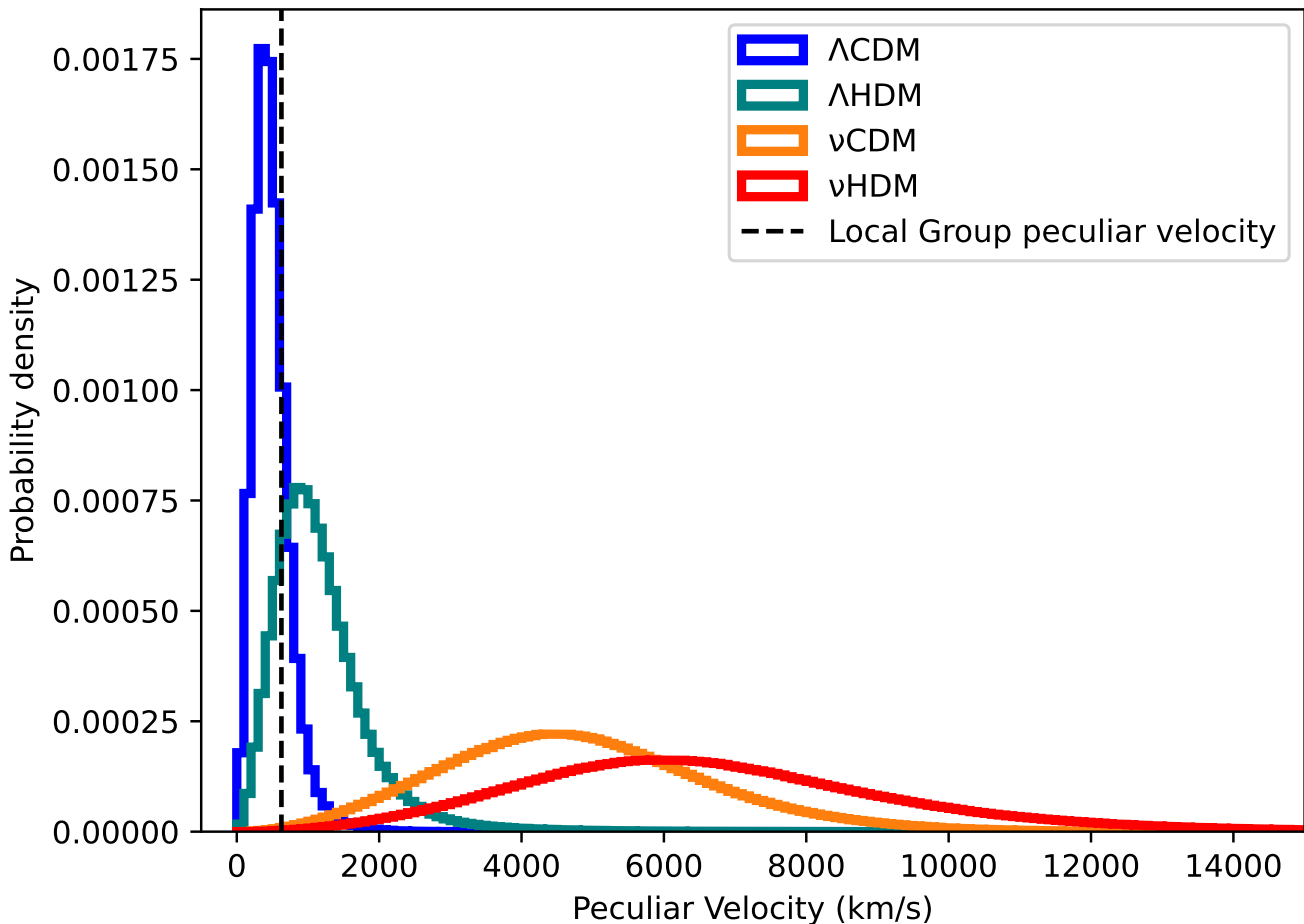


Figure 3. Histograms showing the distribution of particle peculiar velocities in each simulation at $z = 0$. From the leftmost peak to the rightmost peak, these are Λ CDM, Λ HDM, ν CDM, and ν HDM. The Local Group peculiar velocity of 627 km/s is shown for reference using a solid vertical line (Kogut et al. 1993). The typical peculiar velocities in the MOND simulations are thousands of km/s.

(2013) extend out to $800/h_{70}$ Mpc, where $h_{70} \equiv H_0$ in units of 70 km/s/Mpc. This corresponds to $cz = 56000$ km/s or $z = 0.19$, which is sufficient to see the comoving galaxy luminosity density reach a flat level beyond the KBC void (see their figure 11). This extended flat level allows for accurate normalization of the results within the KBC void. However, as discussed in the introduction to Banik & Kalaitzidis (2025), figure 1 of Wong et al. (2022) shows results out to only $z = 0.08$, by which point the luminosity density is still rising. $z = 0.08$ corresponds to $343/h_{70}$ Mpc in figure 11 of Keenan, Barger & Cowie (2013), which shows that the luminosity density stops rising at this point, making the density here a good estimate of the cosmic average density ρ_0 . However, Wong et al. (2022) assume that the density here is $1.5\rho_0$. Thus, their reported underdensity of the Local Hole ($20 \pm 2\%$) is a significant underestimate. Their published density within the KBC void of $0.8\rho_0$ should actually be rescaled to about $0.8/1.5 = 0.53\rho_0$, which corresponds to a 47% underdensity – almost exactly the same as reported by Keenan, Barger & Cowie (2013). This means there is no disagreement between the results of Keenan, Barger & Cowie (2013) and the less deep results of Wong et al. (2022).

Both studies report results in redshift space, thereby not accounting for RSD. It is difficult for observers to correct for RSD and find the local density contrast more accurately until redshift-

independent distances become available out to ≈ 500 Mpc. We can however quantify the RSD effect in our simulations using an approach similar to section 3.3.2 of HBK20. For this, we construct a parabolic relation between cz and distance r at the background level, neglecting peculiar velocities. We use this to find cz at r_δ and R_δ , reasoning that observers must have counted galaxies within this redshift range because they do not correct for RSD, implicitly assuming a homogeneous expansion. Once we have found the linear and quadratic terms at the background level, we add these on to the contributions from peculiar velocities (Equation 31). This effectively tells us the relation between recession velocity and distance (though it is not accurate to consider redshifts from cosmological expansion as creating a velocity). We next use this relation to obtain r'_δ and R'_δ , the inner and outer limit, respectively, to the distance range the observational galaxy number count actually corresponds to for the given VP. The basic idea is that if a local underdensity inflates the local cz' by 10%, then observers assuming the background redshift-distance relation would find $1.1^3 \times$ fewer galaxies than they might expect based on their assumed volume (neglecting the quadratic term). In general, the ratio between the expected and actual volumes is

$$f_{\text{model}} = \frac{R_\delta^3 - r_\delta^3}{R'_\delta{}^3 - r'_\delta{}^3}. \quad (50)$$

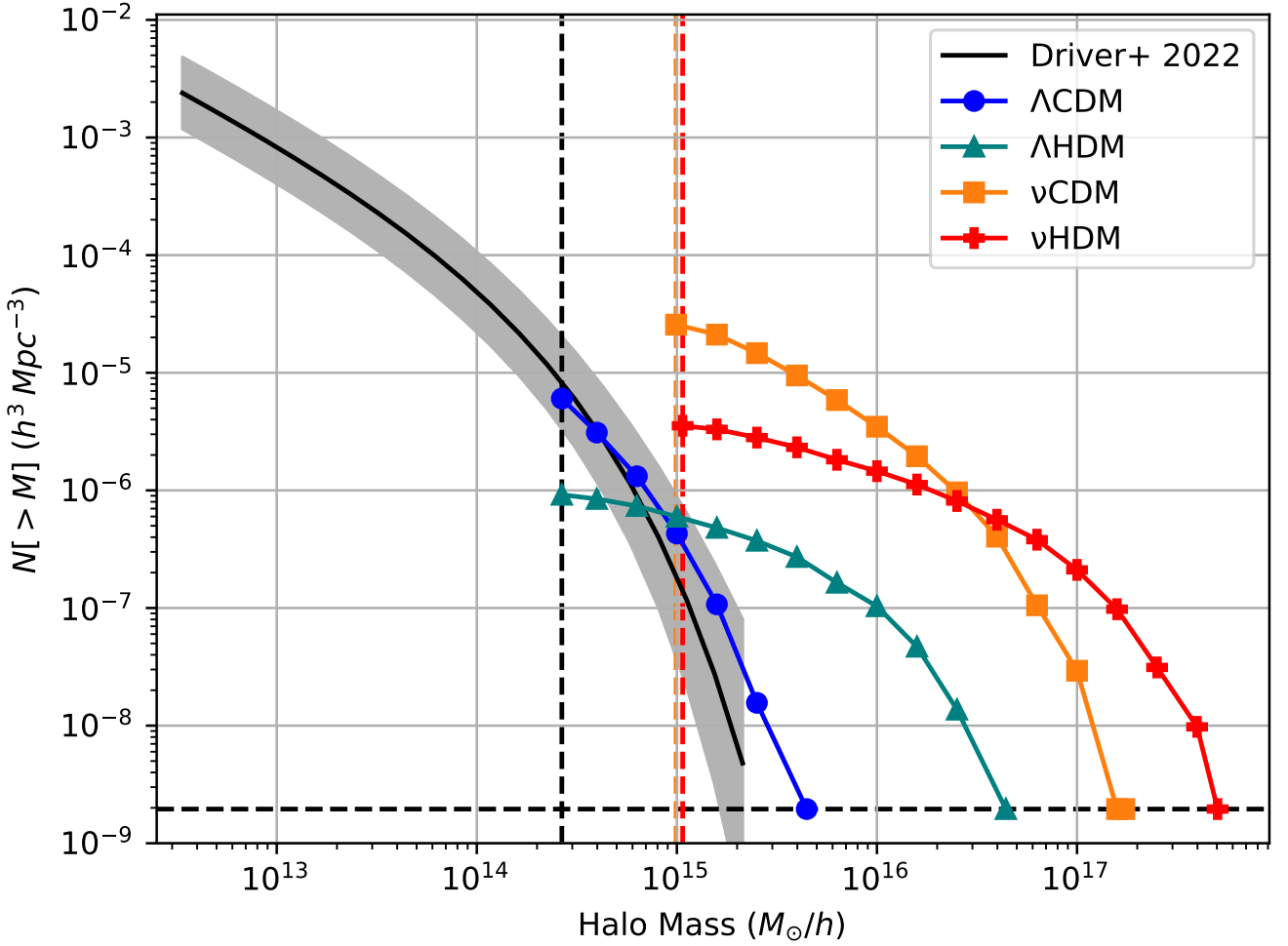


Figure 4. The solid lines with markers show the cumulative halo mass function (CHMF) of each simulation at $z = 0$, as indicated in the legend. The first and last markers represent the lightest and heaviest halo mass in each simulation, whilst the other markers denote intervals of 0.2 dex in mass. The black solid line shows the CHMF observed by [Driver et al. \(2022\)](#) extrapolated to $z = 0$, with the shaded region representing the 1σ confidence interval. The dashed vertical lines represent the minimum halo mass in each simulation, with the MOND simulations having a higher minimum mass due to the use of Newtonian dynamical masses ([Equation 15](#)). Poisson uncertainties on simulation results are too small to be visible here. Λ CDM fits the high mass end of the observations, whilst the Λ HDM and MOND simulations appear to overproduce large structures.

We can then apply the RSD correction as follows:

$$(1 - \delta_{\text{app}}) = (1 - \delta) f_{\text{model}}, \quad (51)$$

where δ is the actual underdensity in the simulation and δ_{app} is the apparent underdensity in redshift space accounting for RSD.

The results obtained with and without correcting the density contrasts in this way are shown in [Figure 5](#). Correcting for RSD allows a more direct comparison with the $\delta_{\text{app}} = 46 \pm 6\%$ underdensity reported by [Keenan et al. \(2013\)](#), which we show in all panels as a solid black line with grey shaded uncertainty band. The simulated distribution is much narrower in Λ CDM, but we use the same bins in δ_{app} in all panels for ease of comparison. It is clear that Λ CDM cannot explain the observed δ_{app} , though interestingly Λ HDM comes fairly close despite using Newtonian gravity. We attribute this to the model having more power on large scales to compensate for the lack of power on small scales given the lack of CDM. A similar broadening is also apparent in the MOND models when going from ν CDM to ν HDM. This broadening allows ν HDM to readily explain the observed δ_{app} , while ν CDM can only marginally do so. The

ability of only the models based on MOND gravity to match the observed δ_{app} provides a strong argument for enhanced structure formation on $\gtrsim 100$ Mpc scales (see also [HBK20](#)).

4.4 Bulk Flows

Having explored the local density field, we now turn to the local velocity field as traced by the bulk flow curve in each simulation ([Section 3.3](#)). At each scale, we show the distribution of values across different VPs using the mean and standard deviation ([Figure 6](#)). The observed bulk flows from [Watkins et al. \(2023\)](#) lie well above expectations in Λ CDM, as quantified in their figure 8. The observed bulk flow is most in line with the Λ HDM model, with ν CDM appearing to predict too large bulk flows. This is even more so for ν HDM, which predicts that a typical observer should see a bulk flow about $10\times$ larger than observed.

As we go to larger scales, the bulk flow becomes smaller in all panels of [Figure 6](#). This is to be expected because the universe becomes more homogeneous on larger scales in all our models. The

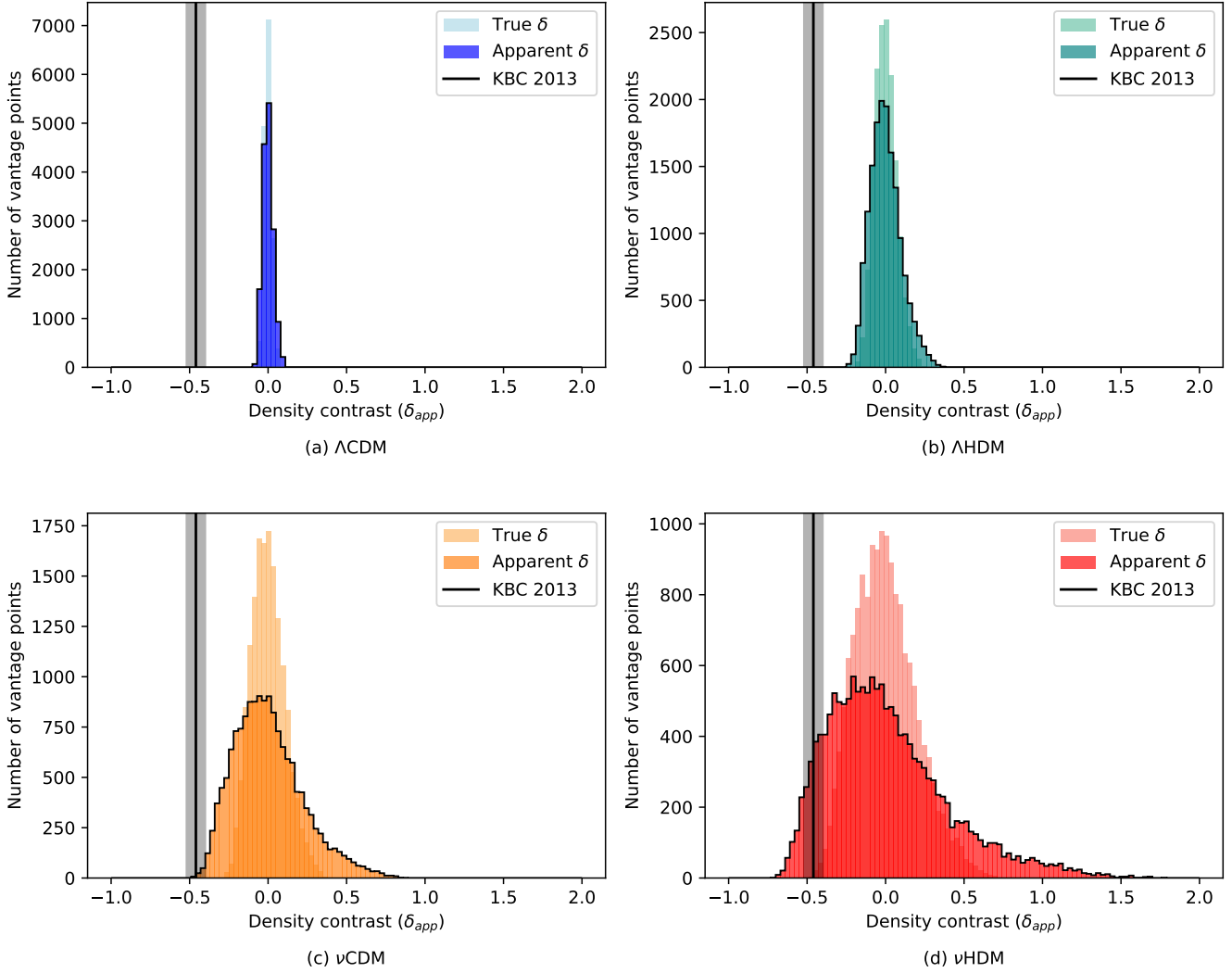


Figure 5. Histograms showing the local density contrast at $z = 0$ within $225/h$ Mpc of each VP for our simulation of Λ CDM (top left), Λ HDM (top right), ν CDM (bottom left), and ν HDM (bottom right). Each panel contains two histograms, with the lighter histogram representing the true density contrast and the darker histogram with a black edge representing the apparent (RSD corrected) density contrast an observer would measure (Equation 51). The apparent density contrast measured by Keenan et al. (2013) is shown as a solid black vertical line, with uncertainty indicated using the grey shaded band. The same bins are used in all panels to make comparison easier.

Simulation	Percentage of VPs which fit observed bulk flow curve		
	1σ	3σ	5σ
Λ CDM	< 0.01%	< 0.01%	< 0.01%
Λ HDM	0.13%	0.99%	2.45%
ν CDM	< 0.01%	< 0.01%	0.03%
ν HDM	< 0.01%	< 0.01%	< 0.01%

Table 2. Percentage of bulk flow curves in each simulation with a better than 1σ , 3σ , or 5σ fit to the observed bulk flow curve (Watkins et al. 2023). Those marked < 0.01% had no matching VPs in our simulations, indicating a fraction < 25^{-3} .

expected declining trend is however not observed (Watkins et al. 2023). Our simulations suggest that extending the observations out to larger radii will show a declining bulk flow (as also suggested by the cosmic dipole in radio source counts above some flux threshold; Wagenveld et al. 2024). Since the results shown in Figure 6 are across all VPs, it may be possible to find some VPs where the bulk flow curve is locally rising, an issue we turn to next.

We consider the bulk flow curve at each VP out to $200/h$ Mpc, beyond which the observational results are less reliable (Watkins et al. 2023). In particular, the reduced number density of observed galaxies beyond this distance can lead to artificial flattening of the bulk flow curve. We then consider the χ^2 of the simulated bulk flow curve with respect to the observations. We convert the likelihood of a higher χ^2 into a Gaussian equivalent tension for a single variable. In this way, we quantify the proportion of VPs in each simulation for which the observed bulk flow curve is fit to better than 1σ , 3σ , and 5σ . The results are shown in Table 2. It is clear that rising bulk flow curves similar to that observed can sometimes arise in a simulation that becomes more homogeneous on large scales. The most successful simulation in this respect is Λ HDM, with Λ CDM producing bulk flows that are too small and the MOND models producing bulk flows that are too large. This problem is particularly acute for ν HDM. Our results suggest that the Watkins et al. (2023) rising bulk flow curve is realistic given the initial conditions imprinted by the CMB, but only if structure

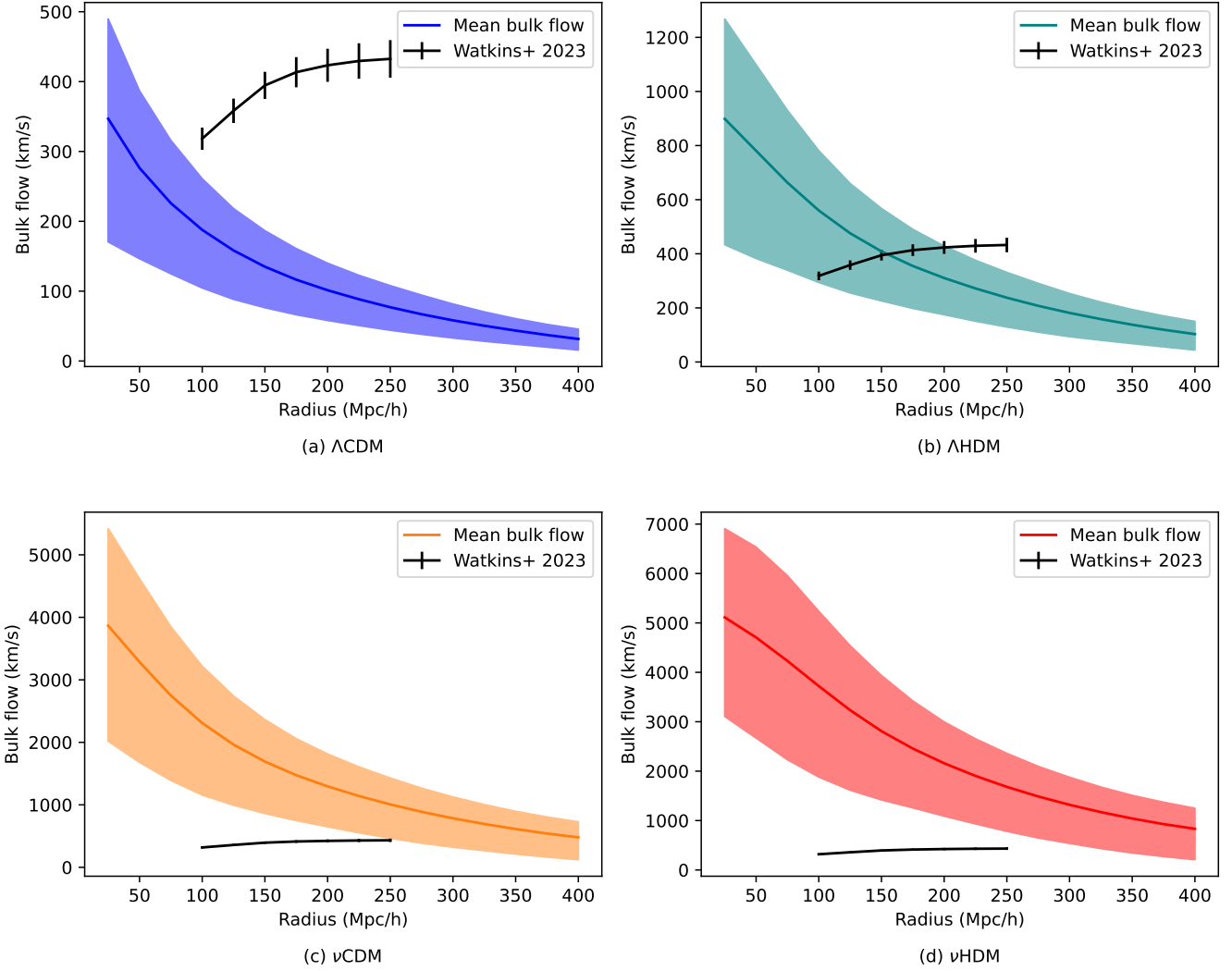


Figure 6. Mean bulk flows for Λ CDM (top left), Λ HDM (top right), ν CDM (bottom left), and ν HDM (bottom right). The shaded regions represent the standard deviation from the mean, while the black line with error bars shows the observed local bulk flow (Watkins et al. 2023). All simulations show a decreasing trend for bulk flow with radius. Λ CDM predicts much smaller bulk flows than observed at large radii, whilst the MOND simulations seem to overpredict the bulk flows, especially at low radii. Bulk flows in Λ HDM seem to have speeds comparable to the observations.

formation on the relevant $\gtrsim 100$ Mpc scales is enhanced somewhat compared to Λ CDM. This enhancement should be far smaller than in ν HDM, which cannot be considered a realistic description of the local Universe.

4.5 Hubble tension and deceleration parameter

The Hubble tension provides an important motivation to consider simulations with enhanced structure formation on large scales compared to Λ CDM. This is because the increased cosmic variance in the local cz' would reduce the statistical significance of the mismatch between it and the expected background \dot{a} from CMB observations. Bearing this in mind, we use Figure 7 to show the apparent local Hubble and deceleration parameters (Section 3.4). These results can be compared with the observed values from Camarena & Marra (2020), which we show towards the bottom right of each panel as a point with uncertainties. All simulations struggle to match the observations, but ν HDM comes closest due to the very wide range of apparent deceleration parameters that it produces.

This wide range makes it unlikely that the observed value should be so close to the background value of -0.53 . We attribute this issue to the late and rapid growth of structure in ν HDM. Our results suggest that the observed local underdensity would have built up much more gradually over most of the Hubble time, whereas in ν HDM, structure formation is fairly slow until accelerations enter the MOND regime at $z \lesssim 50$.

To gain further insight, we colour the result of each VP in Figure 7 according to the apparent density contrast δ_{app} . VPs with a similar δ_{app} define a similar track in the plane of apparent Hubble and deceleration parameters. VPs with a different δ_{app} define a parallel track. Interestingly, the ν HDM track that passes close to the observed point corresponds to $\delta_{app} \approx -0.5$, though given the uncertainties, a somewhat smaller underdensity also seems to fit. The ν HDM model therefore provides a reasonable fit to the observations of Camarena & Marra (2020). This success should be replicated in a different model that enhances structure formation over Λ CDM to a far smaller extent given ν HDM produces too much structure (Figure 6). Out of the models we consider, those based on

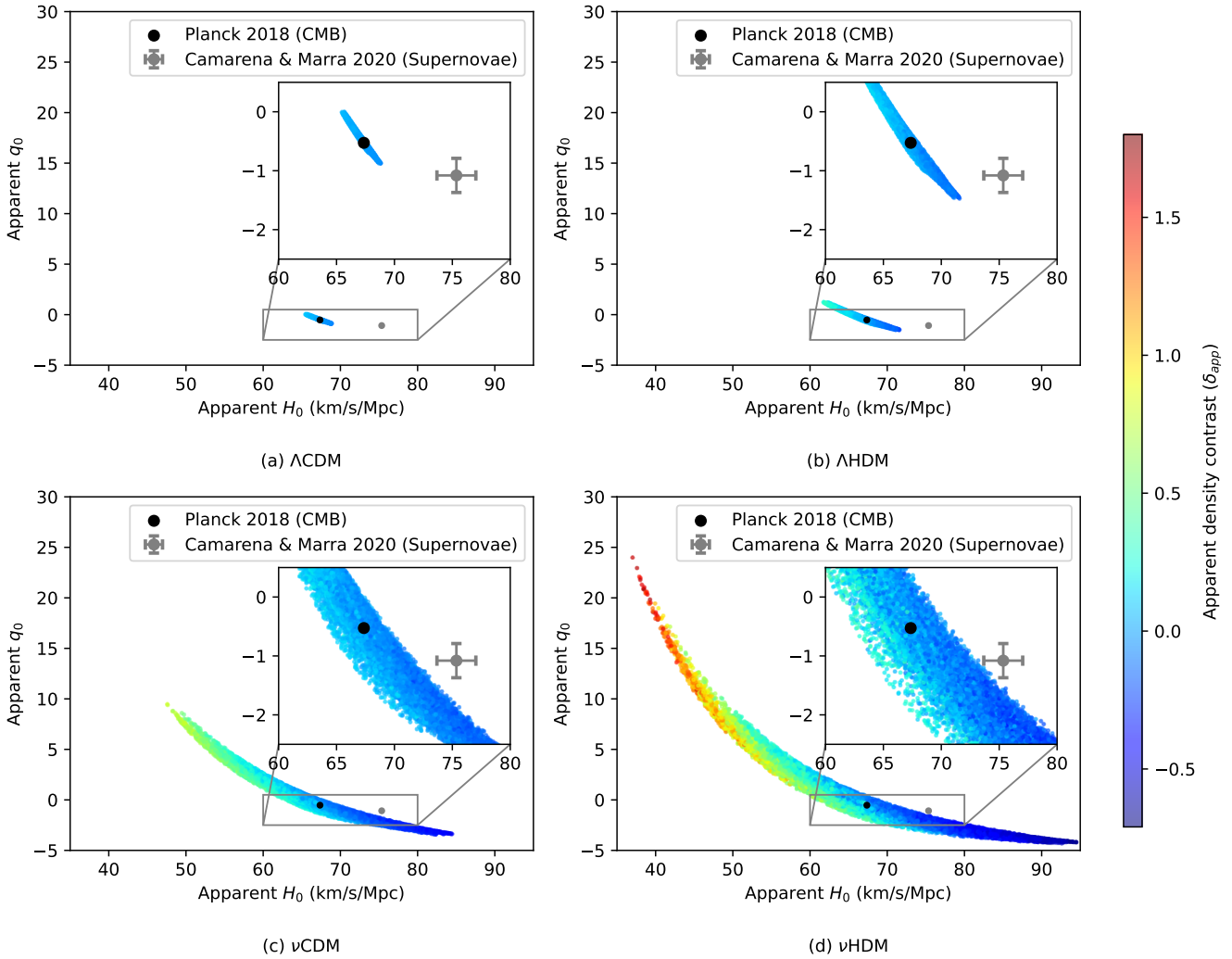


Figure 7. Scatter plots of $q_{0,app}$ vs $H_{0,app}$ for each VP in our simulation of Λ CDM (top left), Λ HDM (top right), ν CDM (bottom left), and ν HDM (bottom right). Markers are coloured according to the apparent density contrast about the VP. The values measured by Camarena & Marra (2020) and Planck Collaboration VI (2020) are shown for reference, with a zoom-in included to make observational uncertainties visible.

GR are not capable of achieving this, but those based on MOND come fairly close, with both ν CDM and ν HDM capable of solving the Hubble tension.

4.6 Hubble Dipole

The velocity field in the local Universe can also be quantified in terms of the apparent dipole in H_0 (Section 3.5). A detection was claimed by Migkas et al. (2021) using galaxy clusters, whose relative distances can supposedly be found from various scaling relations. They use galaxy clusters across a range of redshifts, with the typical redshift corresponding to a distance of about $350/h$ Mpc. The Hubble dipole (direction of highest H_0) is reported to lie towards $l = 93^\circ$, $b = 11^\circ$ in Galactic coordinates. This is almost opposite to the bulk flow of galaxies on smaller scales ($l = 298^\circ$, $b = -8^\circ$; Watkins et al. 2023). Since redshifts are inflated parallel to a bulk flow, we would expect the Hubble dipole to roughly align with the bulk flow on slightly smaller scales. Instead, the dot product between the above two directions is $\cos \theta_{obs} = -0.91$, indicating almost completely the opposite.

To quantify the likelihood of $\cos \theta \approx -1$ in our simulations, we use Figure 8 to show $\cos \theta$ between the bulk flow out to $200/h$ Mpc and the Hubble dipole out to $350/h$ Mpc. Our results confirm that $\cos \theta$ is generally close to +1. A larger angle than reported observationally (lower $\cos \theta$) is very rare, arising about 0.3% of the time (2.75σ tension). This result is fairly consistent across all considered simulations, presumably because $\cos \theta$ is a function of rather large-scale modes in the initial conditions, which are similar between the different models.

The reported dipole amplitude of $9.0 \pm 1.7\%$ is also very rare in our simulations, as seen from the joint distribution of $\cos \theta$ and the percentage Hubble dipole (Figure 9). The ν HDM simulation produces the largest dipoles, but it almost never yields dipoles $\gtrsim 5\%$, not even half the value reported by Migkas et al. (2021).

Our results suggest that their claimed Hubble dipole is unlikely to be sourced by a large-scale bulk flow. The flip in direction and large amplitude at such a large distance appear to be rare in models with initial conditions and a background cosmology similar to those outlined by Planck Collaboration VI (2020). Moreover, the claimed dipole of Migkas et al. (2021) is in the opposite direction to several

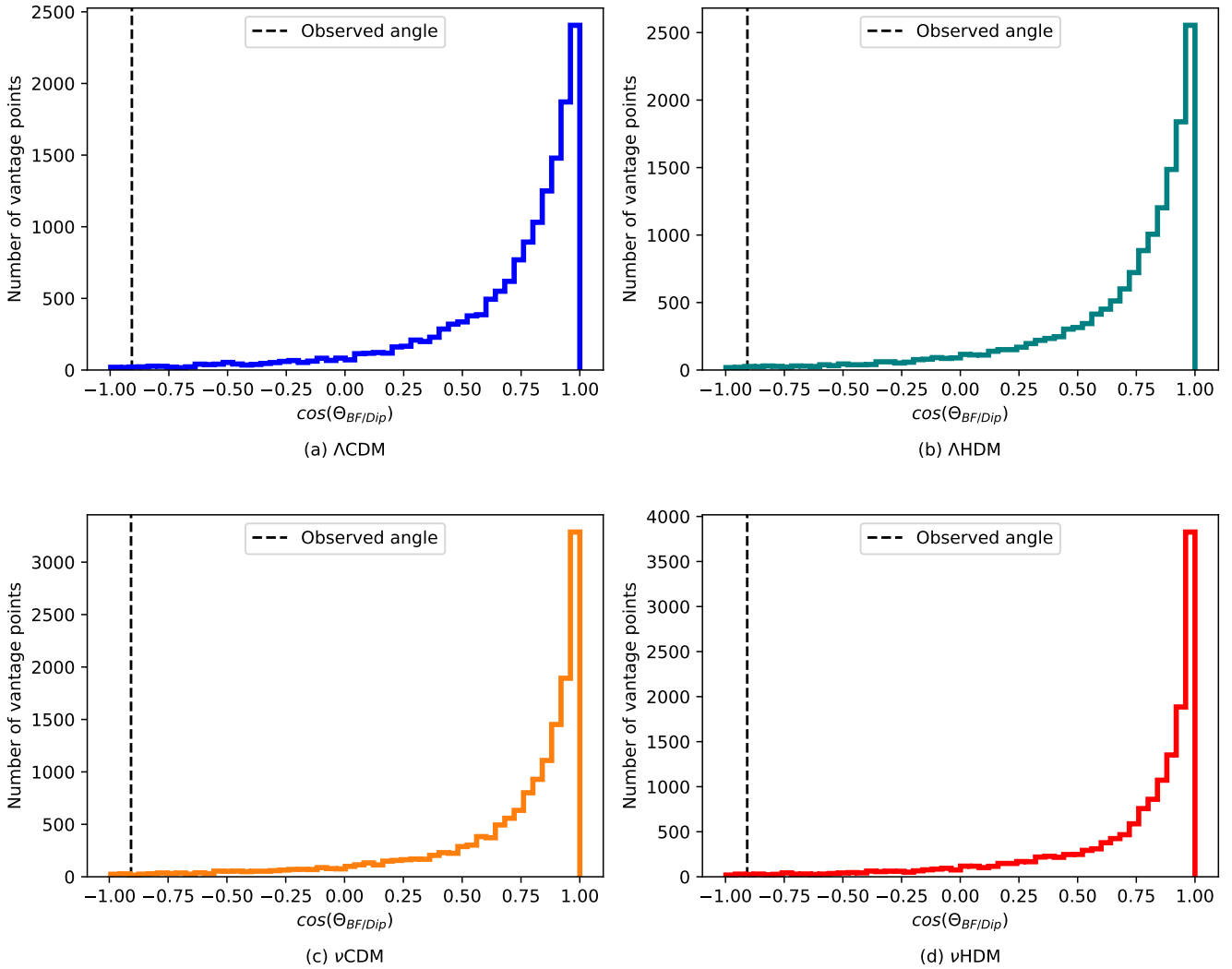


Figure 8. Histograms showing $\cos \theta$ between the bulk flow out to $200/h$ Mpc and the apparent Hubble dipole at $350/h$ Mpc in our simulation of Λ CDM (top left), Λ HDM (top right), ν CDM (bottom left), and ν HDM (bottom right). $\cos \theta = +1$ indicates alignment, while -1 indicates anti-alignment. The black dashed line is the observed angle (Migkas et al. 2021; Watkins et al. 2023). This is rarely reproduced in any simulation.

other studies (Peebles 2022, and references therein), suggesting that the problem may lie with the novel use of galaxy cluster scaling relations as distance indicators (Migkas et al. 2021). A recent detailed analysis has found that there is no statistically significant evidence for anisotropy in these scaling relations, limiting the magnitude of anisotropy in the local cz' to $< 3.2\%$ and the corresponding bulk flow amplitude to < 1300 km/s (Yasin et al. 2026).

5 DISCUSSION

Our results in Figure 4 indicate that the MOND cosmologies we consider produce far too much structure in a Hubble time, as seen in earlier simulations (Angus & Diaferio 2011; Angus et al. 2013). This contradicts expectations from HBK20 that combining HDM with MOND gravity would give approximately the correct amount of structure. Instead, the ν HDM paradigm appears to suffer from the flaws of both Λ CDM and MOND in a ‘worst of both worlds’ scenario – galaxies form far later due to the lack of CDM (Section 5.1; see also Wittenburg et al. 2023), but there would be far too much structure

on large scales by $z = 0$. Since MOND is not compatible with a large amount of CDM, the anomalies in galaxy clusters and the CMB most likely need to be explained using HDM (Banik & Zhao 2022, and references therein). This inevitably leads to a top-down structure formation scenario in which large structures form first and then fragment into smaller structures (Bode, Ostriker & Turok 2001). Gravitational accelerations from structure in the universe become $\lesssim a_0$ when $z \lesssim 50$ (section 3.1.3 of HBK20). This gives a vast amount of time between $z = 50$ and the present epoch for MOND to enhance the growth of structure. The end result is a massive overprediction of peculiar velocities, regardless of whether we use CDM or HDM (Figure 3). This invalidates simple hybrid models of MOND + DM, including ν HDM.

Our results should not be taken to favour the Λ CDM paradigm given the serious difficulties that it faces. In particular, there is the well-known Hubble tension, a $> 5\sigma$ mismatch between the local cz' and the predicted $\dot{a} = H_0^{\text{Planck}}$ from calibrating Λ CDM to the CMB anisotropies (H0DN Collaboration 2025; Di Valentino et al. 2025). The local cz' is most strongly constrained by the Type Ia supernovae distance ladder and seems to be insensitive to

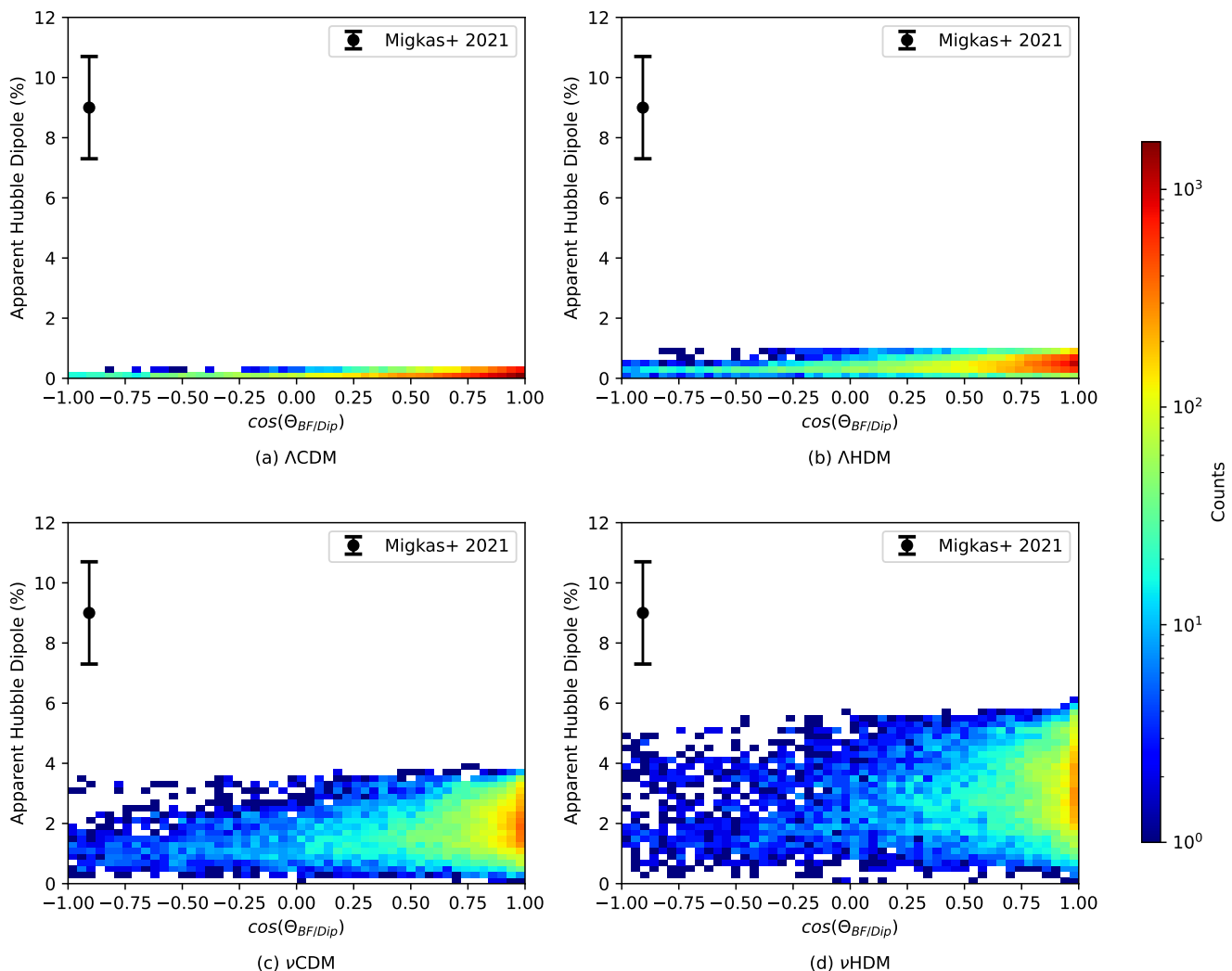


Figure 9. Heatmaps of the apparent Hubble dipole and the angle between it and the bulk flow in our simulation of Λ CDM (top left), Λ HDM (top right), ν CDM (bottom left), and ν HDM (bottom right). The black point with error bars shows the observed quantities (Migkas et al. 2021; Watkins et al. 2023). Changing CDM to HDM and changing from GR to MOND both increase the maximum apparent Hubble dipole. Even so, none of the simulations are able to reproduce the magnitude of the Hubble dipole reported by Migkas et al. (2021). Their reported anti-alignment between the Hubble dipole and bulk flow curve is also quite rare in our simulations.

the distance calibration technique (Uddin et al. 2024) or improvements to the distance calibrations measured between the *Hubble* and *James Webb Space Telescopes* (Riess et al. 2024; Freedman et al. 2025). Likewise, improved measurements of the CMB temperature anisotropies from both space-based (Planck Collaboration VI 2020) and ground-based (Atacama Cosmology Telescope collaboration 2025; Camphuis et al. 2025) facilities have continued the tension, maintaining it as one of the most pressing issues in modern cosmology. The Hubble tension cannot be due to inaccurate measurements of the CMB anisotropies, since Λ CDM requires a low H_0 to explain the combination of the CMB monopole temperature, primordial light element abundances, and BAO data (Banik & Samaras 2025). Other issues include the the observed properties of the KBC void (Keenan et al. 2013; Wong et al. 2022) and the high redshift, mass, and collision velocity of the El Gordo interacting galaxy clusters, which contradicts Λ CDM for any plausible infall velocity (Asencio, Banik & Kroupa 2021, 2023). The El Gordo and KBC void observations suggest a need to enhance the growth of structure on large

scales (HBK20), as also suggested by the anomalously fast bulk flows reported by Watkins et al. (2023) and confirmed by Whitford, Howlett & Davis (2023).

We can consider our simulations as giving some idea of how a cosmological model might behave if structure formation on large scales is indeed faster than in Λ CDM, in which case the Hubble tension could be solved by outflow from a local void (Keenan et al. 2016; Shanks et al. 2019a,b; Ding et al. 2020; San Martín & Rubio 2023; Cai et al. 2025). Some VPs in our MOND models come within $1 - 2\sigma$ of the locally observed values of the Hubble and deceleration parameters, but these typically deviate from the true background values far too much, again highlighting the need for a model which does not depart from Λ CDM as drastically as the ν HDM simulations considered here (Figure 7). Our results suggest that if a local void is to solve the Hubble tension, then the under-density needs to grow steadily rather than rapidly accelerate when $z \lesssim 50$, as happens in ν HDM. In particular, this should lead to a deceleration parameter that deviates less from the background value,

thereby agreeing better with the observations. Since our MOND models produce far too much structure, it is quite plausible that a different model which deviates from Λ CDM to a smaller extent is still able to form analogues to the KBC void frequently enough that it does not falsify the model. Indeed, the KBC void might well be not that common in the correct cosmological model. We note that the deviations from Λ CDM needed to form the KBC void must be associated with the growth of structure because its 300 cMpc scale is very well observed in the CMB power spectrum, where there is excellent agreement with the expected temperature fluctuations (the corresponding multipole moment is about 500; Planck Collaboration VI 2020; Tristram et al. 2024).

5.1 When galaxies form without CDM

It has previously been argued that some form of DM is required even in MOND (Angus 2009; Haslbauer et al. 2020; Banik & Zhao 2022). The tight RAR in rotating disc galaxies suggests that galaxies are purely baryonic and lack CDM (Li et al. 2018; Desmond 2023). However, CDM is an important ingredient in standard galaxy formation theory (White & Rees 1978). It is therefore important to explore whether galaxies can form in a realistic timeframe without CDM, but with the gravity law altered to MOND.

Simple analytic estimates prior to accurate CMB observations suggested that galaxies should form in MOND cosmologies by $z = 10$ (Sanders 1998, 2008), in good agreement with recent observations of early massive galaxies observed by the *JWST* (McGaugh et al. 2024). However, detailed hydrodynamical cosmological ν HDM simulations found that galaxies only form by $z = 4$ in this model (Wittenburg et al. 2023). Those authors carefully considered the initial power spectrum, which is suppressed on the comoving scales of galaxies due to the lack of CDM (see their figure 2). We show below that this discrepancy is driven by differences in the respective background cosmologies.

For a spherical region of radius λ_c with corresponding mass M_c , equation 7 of Sanders (2008) predicts that density fluctuations in the MOND regime during the matter-dominated era will grow to unity at a redshift

$$z_1 = \left(\frac{27}{4a_0} \Omega \lambda_c H_0^2 \right)^{-1/2} - 1, \quad (52)$$

where Ω is the density parameter of the collapsing matter. λ_c and M_c are related by

$$\lambda_c = \sqrt[3]{\frac{3M_c}{4\pi\rho_0}}, \quad (53)$$

where ρ_0 is the background density of the collapsing matter at $z = 0$. Equation 52 can therefore be further generalised as

$$z_1 = \left(\frac{27}{4a_0} \right)^{-1/2} \left(2GH_0^4 \right)^{-1/6} (M_c)^{-1/6} (\Omega)^{-1/3} - 1. \quad (54)$$

Interestingly, this formula is largely independent of the initial fluctuation amplitude. This is visualised in Figure 1 of Sanders (2008), which states that ‘‘MOND drives structure growth towards $(1+z)^{-2}$ quite independently of the initial conditions.’’ They also used a spherically symmetric N -body code to show that these perturbations collapse to form galaxies within ≈ 1 Gyr of reaching unity.

To obtain these promising results, Sanders (2008) assumed a flat FRW cosmology without dark matter such that $\Omega_{dm} = 0$, $\Omega_b = 0.04$, and $\Omega_\Lambda = 0.96$ for, respectively, the dark matter, baryon, and dark energy density in units of the critical density, with a low

present expansion rate of $H_0 = 63$ km/s/Mpc. They assumed a MOND acceleration parameter of $a_0 = 1 \times 10^{-10}$ m/s², very similar to the modern value. With these parameters (and setting $\Omega = \Omega_b$), a benchmark perturbation mass of $M_c = 10^{11} M_\odot$ will reach unity at $z \approx 40$ according to Equation 54. The corresponding redshift of galaxy formation ≈ 1 Gyr later is $z \gtrsim 10$.

We can now compare how a density perturbation of the same mass evolves within this framework for the ν HDM cosmology simulated by Wittenburg et al. (2023). We will assume that density perturbations on galactic scales are baryonic only. Free-streaming of the HDM prevents the growth of perturbations of this component on galactic scales by design – this effect can be seen in figure 10 of Wittenburg et al. (2023), where structures below a mass of $10^{12} M_\odot$ contain virtually no HDM. This approach is theoretically valid as Equation 52 assumes MOND effects apply to perturbations with respect to the background density, which only affects the growth of perturbations through its contribution to the background expansion rate.

The cosmological parameters in the ν HDM model are taken directly from Planck Collaboration VI (2020), i.e., $\Omega_{dm} = 0.266$, $\Omega_b = 0.049$, $\Omega_\Lambda = 0.685$, and $H_0 = 67.4$ km/s/Mpc. The MOND acceleration parameter is also slightly different at $a_0 = 1.2 \times 10^{-10}$ m/s². Setting $\Omega = \Omega_b$ (since only baryonic perturbations will collapse on galactic scales) and again using a benchmark perturbation mass of $M_c = 10^{11} M_\odot$ gives a similar redshift of $z \approx 40$ for the density contrast to reach order unity. However, the higher Ω_m in this model leads to a higher dz/dt at high z , so the redshift of galaxy formation ≈ 1 Gyr later is now $z \gtrsim 5.4$. This is more in line with the redshift of the first galaxies reported by Wittenburg et al. (2023) in their hydrodynamical cosmological ν HDM simulations.

Comparing the age of the universe between both models highlights this difference. In the Sanders (2008) cosmology, the universe is ≈ 0.18 Gyr old at $z = 40$ and ≈ 1.36 Gyr old at $z = 10$. Meanwhile, the Wittenburg et al. (2023) cosmology is only ≈ 0.06 Gyr old at $z = 40$ and ≈ 0.47 Gyr old at $z = 10$. This would leave only 400 Myr for order unity perturbations to collapse, dynamically relax, and then form galaxies by $z = 10$.

We note here that the redshift when the first galaxies form in ν HDM (≈ 5.4 analytically and ≈ 4 from Wittenburg et al. 2023) are both approximate and would require more detailed calculations to confirm. The analytic estimate is likely an upper bound on redshift. Whilst density perturbations with the same λ_c will converge to the same amplitude at a given redshift regardless of their initial amplitude, this convergence is not instantaneous and occurs later for perturbations with lower initial amplitude (see figure 1 of Sanders 2008). The time for perturbations to collapse and virialise after reaching unity should still be ≈ 1 Gyr as the calculations by Sanders (2008) assume the collapsing region has decoupled from the background cosmology. We note that a mass of $10^{11} M_\odot$ lies near the resolution of our simulations. The halo finder used also assumes Newtonian gravity, so the earliest structures were likely gravitationally bound before $z = 4$. Even so, it is difficult to understand how galaxies can form by $z = 14$.

Whilst beyond the scope of this work, a more involved application of the Sanders (2008) methodology to the ν HDM framework would allow for a more conclusive test, but we can expect the true value to lie approximately in the range $4 \lesssim z \lesssim 5.5$ with a Planck Collaboration VI (2020) background cosmology. It is clear both theoretically and through simulations that the epoch of galaxy formation depends on the background cosmology for these MOND models. The prediction that galaxies should form by $z = 10$ is not a generic prediction of all cosmologies with MOND; this redshift

is sensitive to the underlying cosmological parameters. The above discussion highlights that a major reason for the high redshift at which galaxies are expected to form in the Sanders (2008) cosmology is that it uses an outdated background cosmology with a far older universe at $z = 10$.

In the case of ν HDM, optimisations to the background cosmology are unlikely to solve this issue. Whilst the cosmologies considered here are based on the Planck Collaboration VI (2020) parameters for simplicity, Samaras et al. (2025) find that a flat “opt- ν HDM” cosmology with $H_0 \approx 55$ km/s/Mpc, $\Omega_{dm} \approx 0.41$, $\Omega_b \approx 0.09$, and $\Omega_\Lambda \approx 0.5$ provides the optimal fit to the CMB power spectrum for the ν HDM model. The high Ω_m is in $> 20\sigma$ disagreement with BAO results from the Dark Energy Spectroscopic Instrument Data Release 2 (DESI DR2), which shows that $\Omega_m = 0.2975 \pm 0.0086$ without combining with any external datasets (DESI Collaboration 2025). It also provides no tangible improvement to when structures form. A $10^{11} M_\odot$ perturbation would reach unity at $z \approx 37$ and would collapse and virialise ≈ 1 Gyr later, when $z \approx 5$.

Low Ω_m models also face other issues, the most obvious being cosmology-independent constraints on the age of the Universe from the ages of the oldest Galactic stars and globular clusters. The Sanders (2008) model has an age of 24 Gyr at $z = 0$. When the first galaxies form at $z \approx 10$, the age is 1.35 Gyr. The oldest stars in such a model would therefore be ≈ 20 Gyr old. However, Cimatti & Moresco (2023) and Tomasetti et al. (2025) find stellar ages in the Milky Way consistent with an ≈ 14 Gyr old Universe once contaminants have been removed (see also Xiang & Rix 2022; Valcin et al. 2021, 2025; Xiang et al. 2025). The high third peak of the CMB temperature anisotropies may also be problematic for such models due to the lack of dark matter, but this issue may be alleviated in newer relativistic MOND formulations (e.g. Skordis & Złošnik 2021, 2022; Blanchet & Skordis 2024; Durakovic & Skordis 2024).

The problem of late galaxy formation will likely be faced by any cosmological model where MOND gravity is applied to density perturbations in an FRW background given the inevitable lack of CDM. For ν HDM specifically, structure is formed too rapidly and too recently, producing too little at early times and too much at late times. The available hydrodynamical cosmological ν HDM simulations indicate that MOND with DM does not produce the high redshift galaxies observed by the *JWST*. This reveals a fundamental problem with the ν HDM paradigm, invalidating it as a viable theory of structure formation.

5.2 Particle physics and cosmology constraints on sterile neutrinos

In our simulations and those of Wittenburg et al. (2023), the HDM component in ν HDM is assumed to be 11 eV sterile neutrinos, as proposed by Angus (2009). None of the ordinary neutrinos can play the role of HDM as their rest energy is at most 0.45 eV (Katrin Collaboration 2019, 2022, 2025). Sterile neutrinos as dark matter was first proposed by Dodelson & Widrow (1994). They are an attractive candidate as they are physically motivated by the standard model of particle physics and are expected to be weakly interacting. However, recent particle physics experiments cast doubt on the existence of sterile neutrinos (KATRIN Collaboration 2025; MicroBooNE collaboration 2025). Whilst the HDM in ν HDM does not necessarily have to be 11 eV sterile neutrinos, the physical motivation for the model is weakened by these null detections.

Another problem with the 11 eV sterile neutrino hypothesis is that these would contribute an extra relativistic degree of freedom

during the BBN era. This would increase the expansion rate, reducing the time between any two fixed temperature thresholds and thus the decay of free neutrons, increasing the primordial helium abundance (Cyburt et al. 2016). Recent results indicate that the effective number of neutrino species during the BBN era was close to the standard value of 3, with 4 excluded at quite high confidence (Kirilova et al. 2024). Since the sterile neutrinos are expected to be thermalised, this is an important issue for the ν HDM paradigm. It could be avoided if the sterile neutrinos were more massive and not fully thermalised during the BBN era, but too high a mass would start to affect galaxies, undermining the MOND rotation curve fits (Angus 2010).

5.3 Constraints on MOND from bound systems

Our simulations show that naively applying MOND to large scales using the Jeans swindle approach (Nusser 2002) and adding HDM to fit galaxy clusters and the CMB leads to results incompatible with the observed large-scale structure. Our results are in line with difficulties faced by MOND in the outskirts of galaxy clusters – even if we were to add the required amount of DM to fit the kinematics in their central regions (Li et al. 2023). This is also evident in figure 5 of Kelleher & Lelli (2024), where the inferred g at low accelerations (large radii) falls below the MOND expectation of $\sqrt{g_N a_0}$.⁵ The results instead suggest that g_N should be enhanced by a fixed factor, which interestingly is similar to Ω_m/Ω_b inferred in Λ CDM using the CMB anisotropies (Planck Collaboration VI 2020; Tristram et al. 2024). This is to be expected if gravity follows the Newtonian inverse square law in the low acceleration regime and the ratio of enclosed baryonic to total matter in galaxy clusters is similar to that in the universe as a whole by the time we get to their outskirts. If a viable MOND + dark matter cosmological model exists, we would need to suppress MOND effects on large scales despite the low accelerations, in order to fit the cluster RAR and the observed CHMF and large-scale structure.

In addition to difficulties faced by MOND in the outskirts of galaxy clusters, it also struggles to match Solar System ephemerides, with Cassini radio tracking data from Saturn orbit falsifying the classical AQUAL and QUMOND modified gravity formulations of MOND at 8.7σ confidence in combination with constraints on a_0 and the interpolating function from galaxy rotation curves (Desmond, Hees & Famaey 2024). The orbital energy distribution of long-period comets and the inclination distribution of Kuiper belt objects have also been used to rule out the AQUAL formulation of MOND (Vokrouhlický, Nesvorný & Tremaine 2024). In particular, the Oort Cloud would not be stable on Gyr timescales in MOND gravity and Kuiper Belt objects would have a much broader range of inclinations to the Ecliptic than is observed, suggesting that MOND effects should be suppressed in the outer Solar System.

There is ongoing controversy on whether the dynamics of wide binary stars in the Solar neighbourhood are consistent with MOND. The groups of Pittordis & Sutherland (2023) and Banik et al. (2024) claim that wide binaries favour Newtonian gravity, in the latter case apparently ruling out MOND at 16σ confidence. However, other studies instead claim that wide binaries favour MOND with an external field effect (Hernandez et al. 2022; Hernandez 2023; Hernandez et al. 2024a; Chae 2023, 2024a,b). For instance, Chae (2024b) found a $6 - 9\sigma$ preference for MOND. A review by Hernandez et al.

⁵ The clusters A644 and A2319 should not be considered due to ongoing merger signatures.

(2024b) has highlighted issues in Pittordis & Sutherland (2023) and Banik et al. (2024) that may have erroneously biased their results towards Newtonian gravity. Of particular concern are the fitting of noise free templates to noisy data in Pittordis & Sutherland (2023), uncertainties that are larger than data bin widths in Banik et al. (2024), the lack of a ‘Newtonian anchor’ regime as a reference in both, and the modelling of hidden tertiary companions. For example, the tertiary companion fraction in Banik et al. (2024) is inferred to be $63 \pm 1\%$ in their nominal analysis (see their table 3), whereas more direct observations find it should be below 50% (e.g., see figure 39 of Moe & Di Stefano 2017). We note that Banik et al. (2024) argued in their section 5.1.3 that further refinements to the unknown distribution of close binary orbital radii could reduce the close binary fraction to perhaps 50%, but even so, the large fraction of close binaries makes it difficult to be sure of the gravity law. There are good prospects for better characterising the close binary population in the near future (Manchanda, Sutherland & Pittordis 2023). This field still appears to be under debate, e.g. Pittordis et al. (2025) address the criticisms of their earlier work and still maintain preference for Newtonian gravity, whilst Chae (2026) apply new data from HARPS and again finds preference for MOND. We also note the appearance of three recent studies that argue local wide binaries favour Newton over MOND (Mahmud Saad & Ting 2025; Makarov 2026; Cookson et al. 2026), with Cookson et al. (2026) suggesting that earlier claims in favour of MOND were driven by selection effects.

Despite some issues and debate on scales smaller and larger than galaxies, MOND is still successful with the internal dynamics of galaxies, including with regards to the tidal stability of dwarf galaxies in cluster environments (Asencio et al. 2022) and the origin of the planes of satellite galaxies in the LG from a past flyby encounter between the Milky Way and Andromeda galaxies (Banik et al. 2018; Bilek et al. 2018; Banik et al. 2022). This flyby is inevitable in MOND (Zhao et al. 2013) and may be testable in future through anisotropy of distant Galactic tidal streams (Asencio, Kroupa & Thies 2025). The asymmetric tidal tails of open star clusters in the Solar neighbourhood have also been argued to favour MOND (Kroupa et al. 2024). These results extend the success of MOND on galaxy scales beyond equilibrium dynamics, with the external field effect playing a crucial role in tidal stability considerations. Galaxy-galaxy weak lensing by isolated lens galaxies down to $g_N \approx 10^{-15} \text{ m/s}^2$ or about $10^{-5} a_0$ also seems to follow MOND predictions (Brouwer et al. 2021; Mistele et al. 2024a,b). It is not presently clear how these results can be understood without the action of a MOND-like force law.

6 CONCLUSIONS

In this work, we present the largest collisionless N -body simulations of a MOND cosmology to date, with a box size of $800/h \text{ cMpc}$ and 256^3 particles. These simulations aimed to compare the Λ CDM standard model of cosmology to the newer ν HDM model (Angus 2009), which combines MOND gravity (ν) with HDM in the form of sterile neutrinos with a rest energy of 11 eV. The resulting cosmology is assumed to have an identical expansion rate history to Λ CDM and adequately fits the CMB power spectrum almost as well as Λ CDM (figure 2 of Wittenburg et al. 2023). The model was also expected to reproduce galaxy cluster dynamics thanks to the HDM component (Angus & Diaferio 2011) and to reproduce MOND fits to galaxy rotation curves given the low density of HDM (Angus et al. 2010). ν HDM has previously been simulated in smaller boxes

of size 256 and 512 Mpc/h (Angus & Diaferio 2011; Angus et al. 2013). For further discussion of the ν HDM paradigm, we refer the reader to section 3.1 of HBK20.

We performed simulations for 4 distinct cosmological models: Λ CDM as a baseline, ν HDM as our physically motivated alternate model, and two unphysical models we dubbed Λ HDM and ν CDM to test the individual effects of using HDM or MOND gravity, respectively. The simulations were set up in a similar manner to that outlined in Wittenburg et al. (2023), with a Planck Collaboration VI (2020) background cosmology. We disabled the hydrodynamical features for our runs, allowing a complementary study where we focus on cosmological aspects of the model in a large simulation box.

We find that the HDM models underproduce light haloes and overproduce massive haloes when compared to their CDM counterparts, consistent with previous simulations (Angus et al. 2013). We also find that the MOND models produce structures at least $10\times$ more massive than their Newtonian counterparts. Our results build on Angus & Diaferio (2011) and Angus et al. (2013) by extending this measurement to larger masses and comparing with updated measurements of the CHMF. The MOND models fail to reproduce observed halo counts from Driver et al. (2022) at the high mass end, where haloes up to $5 \times 10^{17} M_\odot/h$ form in ν HDM by $z = 0$ (Figure 4). This general overproduction of structure is also evident in Figure 3, where the typical peculiar velocities of around 5000 km/s in ν HDM leave the LG peculiar velocity of ‘only’ 627 km/s as a 3.2σ outlier.

We also investigated the formation of supervoids analogous to the observed KBC void (Keenan, Barger & Cowie 2013) or Local Hole (Wong et al. 2022). Such phenomena were already seen to be produced in the ν HDM model (Angus et al. 2013) and could potentially solve the Hubble tension, as outflows from a local supervoid could lead to an overestimation of the locally determined Hubble constant. Such supervoids are readily apparent in ν HDM (Figure 1). When measuring the density contrast within $225/h \text{ Mpc}$ of an observer, we confirm quantitatively that structures analogous to the Local Hole can form in ν HDM (Figure 5). No such analogous underdensities are found in either of the Newtonian simulations.

We then explored the effect of the local density contrast on the locally determined Hubble constant and deceleration parameter (Figure 7). We find all our simulations struggle to exactly match the observed values (Camarena & Marra 2020). In the Newtonian simulations, this is because large enough values of \mathcal{H}_0 are not reached, whereas in the MOND models, the corresponding Q_0 values are too negative. The overproduction of structure in the MOND models is once again evident here in that some regions of our ν HDM simulations have an extreme value of $Q_0 \geq 20$. We also see evidence of the resulting supervoids overcorrecting the Hubble tension, with values ranging between $40 < \mathcal{H}_0 < 100 \text{ km/s/Mpc}$.

We found the MOND models also overcorrect the bulk flow tension (Figure 6). Whereas Λ CDM is ruled out at $> 5\sigma$ confidence due to it *underpredicting* the observed local bulk flow (Watkins et al. 2023), we conversely find ν HDM is ruled out to $> 5\sigma$ confidence by *overpredicting* the bulk flow curve. Ironically, it is only our ‘unphysical’ Λ HDM model that appears to match this observation well, although this is likely a fluke simply due to the higher peculiar velocity field present in this model compared to Λ CDM.

The final cosmological tension we explored was the Hubble dipole observed by Migkas et al. (2021). If this dipole is sourced by some large scale bulk flow, it must have reversed direction compared to the bulk flow measured by Watkins et al. (2023) on a slightly smaller scale. We find such a reversal to be rare across all of our

simulations, with the dipole magnitude also being unreproducible if sourced by a bulk flow. We therefore suggest that a bulk flow origin for the dipole should be dismissed as it would evidently require a cosmological model more extreme than even the ν HDM model. Regardless of the cosmological model, it is important to understand why the Hubble dipole reported by Migkas et al. (2021) is in the opposite direction to most other studies (Peebles 2022).

We also discussed when the first galaxies are predicted to form in ν HDM using the analytic formulae of Sanders (2008). We found that with a flat background cosmology in which $\Omega_m \approx 0.3$ and $H_0 \approx 70$ km/s/Mpc, the first galaxies are not expected to form before $z = 5$ in a ν HDM-like model. This prediction is consistent with the formation of the first galaxies at $z \approx 4$ in the hydrodynamical ν HDM simulations of Wittenburg et al. (2023). Such models will therefore be unable to form the high redshift galaxies observed by *JWST* at $z \gtrsim 14$ (Carniani et al. 2024). The main reason for Sanders (2008) predicting such high redshift galaxies appears to be the use of an outdated background cosmology in which there is much more time at $z > 14$, but this also leads to a far older universe at $z = 0$, in tension with the ages of the oldest Galactic stars and globular clusters. A generic consequence of MOND is an absence of CDM, which can make it very difficult to form galaxies at high redshift.

Taking these results as a whole, we argue that ν HDM, or any derivative thereof, can be discounted as a viable alternative cosmological model. We find the tension at the high mass end of the CHMF is worsened as the observations probe to higher masses (Driver et al. 2022) and that the typical peculiar velocities are an order of magnitude too high. The model also fails to solve key cosmological tensions for Λ CDM. The bulk flow tension is overcorrected, allowing us to reject ν HDM at $> 5\sigma$ confidence based on this alone. Whilst the model does successfully produce analogues to the Local Hole (Wong et al. 2022), this does not lead to a satisfactory supervoid solution to the Hubble tension. The observed Hubble dipole (Migkas et al. 2021) is also not reproduced. It appears that whenever the eventual solution(s) to these tensions is discovered, it will take the form of a much more subtle modification to the Λ CDM paradigm than the ν HDM cosmology.

ACKNOWLEDGEMENTS

The authors would like to thank the referee, whose comments have significantly improved the scientific content of this work. AR is supported by studentship ST/X508780/1 from the Science and Technology Facilities Council. IB is supported by Royal Society University Research Fellowship grant 211046. IB and HZ were supported by Science and Technology Facilities Council grant ST/V000861/1. OC was supported by a grant from the Student-Staff Council (SSC) and Physics Trust at the department of physics and astronomy at the University of Saint Andrews, as well as the Saint Andrews Research Internship Scheme (StARIS). HZ acknowledges the Fellowship for international cooperation from the University of Science and Technology of China, and a visiting professorship from Imperial College London. The authors are grateful to Stacy McGaugh and the HPC team at Case Western Reserve University for providing access to and aid with their computing cluster, on which the simulations were run. The authors would also like to thank Harry Desmond for helpful comments.

DATA AVAILABILITY

Nagesh et al. (2021) provides a user guide for FOR, with the linked online repository containing the cosmological patch used in this contribution. The techniques used here are similar to Wittenburg et al. (2023), with the simplification that we do not consider baryonic physics processes. Halo catalogues can be made available upon reasonable request.

REFERENCES

- Aalbers J., et al., 2025, *Physical Review Letters*, **134**, 241801
 Abazajian K., 2006, *Physical Review D*, **73**, 063506
 Angulo R. E., Springel V., White S. D. M., Jenkins A., Baugh C. M., Frenk C. S., 2012, *MNRAS*, **426**, 2046
 Angus G. W., 2009, *MNRAS*, **394**, 527
 Angus G. W., 2010, *JCAP*, **2010**, 026
 Angus G. W., Diaferio A., 2011, *MNRAS*, **417**, 941
 Angus G. W., Shan H. Y., Zhao H. S., Famaey B., 2007, *ApJ*, **654**, L13
 Angus G. W., Famaey B., Diaferio A., 2010, *MNRAS*, **402**, 395
 Angus G. W., Diaferio A., Kroupa P., 2011, *MNRAS*, **416**, 1401
 Angus G. W., Diaferio A., Famaey B., van der Heyden K. J., 2013, *MNRAS*, **436**, 202
 Arora N., Courteau S., Stone C., Macciò A. V., 2023, *MNRAS*, **522**, 1208
 Asencio E., Banik I., Kroupa P., 2021, *MNRAS*, **500**, 5249
 Asencio E., Banik I., Mieske S., Venhola A., Kroupa P., Zhao H., 2022, *MNRAS*, **515**, 2981
 Asencio E., Banik I., Kroupa P., 2023, *ApJ*, **954**, 162
 Asencio E., Kroupa P., Thies I., 2025, *A&A*, **702**, A62
 Atacama Cosmology Telescope collaboration 2025, *JCAP*, **2025**, 062
 Banik I., Kalaitzidis V., 2025, *MNRAS*, **540**, 545
 Banik I., Samaras N., 2025, *Astronomy*, **4**, 24
 Banik I., Zhao H., 2018, *MNRAS*, **480**, 2660
 Banik I., Zhao H., 2022, *Symmetry*, **14**, 1331
 Banik I., O’Ryan D., Zhao H., 2018, *MNRAS*, **477**, 4768
 Banik I., Haslbauer M., Pawlowski M. S., Famaey B., Kroupa P., 2021, *MNRAS*, **503**, 6170
 Banik I., Thies I., Truelove R., Candlish G., Famaey B., Pawlowski M. S., Ibata R., Kroupa P., 2022, *MNRAS*, **513**, 129
 Banik I., Pittordis C., Sutherland W., Famaey B., Ibata R., Mieske S., Zhao H., 2024, *MNRAS*, **527**, 4573
 Begeman K. G., Broeils A. H., Sanders R. H., 1991, *MNRAS*, **249**, 523
 Bhardwaj A., Matsunaga N., Huang C. D., Riess A. G., Rejkuba M., 2025, *ApJ*, **990**, 63
 Bílek M., Thies I., Kroupa P., Famaey B., 2018, *A&A*, **614**, A59
 Biviano A., 2006, in Mamon G. A., Combes F., Deffayet C., Fort B., eds, *EAS Publications Series Vol. 20*, EAS Publications Series. EDP, pp 171–178 ([arXiv:astro-ph/0509679](https://arxiv.org/abs/astro-ph/0509679)), doi:10.1051/eas:2006066
 Blanchet L., Skordis C., 2024, *JCAP*, **2024**, 040
 Bode P., Ostriker J. P., Turok N., 2001, *ApJ*, **556**, 93
 Brouwer M. M., et al., 2021, *A&A*, **650**, A113
 Cai T., Ding Q., Wang Y., 2025, *Physical Review D*, **111**, 103502
 Camarena D., Marra V., 2020, *Physical Review Research*, **2**, 013028
 Camphuis E., et al., 2025, preprint, *Arxiv* ([arXiv:2506.20707](https://arxiv.org/abs/2506.20707))
 Candlish G. N., 2016, *MNRAS*, **460**, 2571
 Candlish G. N., Smith R., Fellhauer M., 2015, *MNRAS*, **446**, 1060
 Carniani S., et al., 2024, *Nature*, **633**, 318
 Cavaliere A., Fusco-Femiano R., 1976, *A&A*, **49**, 137
 Chae K.-H., 2023, *ApJ*, **952**, 128
 Chae K.-H., 2024a, *ApJ*, **960**, 114
 Chae K.-H., 2024b, *ApJ*, **972**, 186
 Chae K.-H., 2026, *ApJL*, **998**, L43
 Chae K.-H., Bernardi M., Domínguez Sánchez H., Sheth R. K., 2020, *ApJ*, **903**, L31
 Cimatti A., Moresco M., 2023, *ApJ*, **953**, 149
 Colín P., Valenzuela O., Avila-Reese V., 2008, *ApJ*, **673**, 203

- Cookson S. A., Banik I., El-Badry K., Sutherland W., Penoyre Z., Pittordis C., Clarke C. J., 2026, *MNRAS*, in press
- Crain R. A., et al., 2015, *MNRAS*, 450, 1937
- Cybart R. H., Fields B. D., Olive K. A., Yeh T.-H., 2016, *Reviews of Modern Physics*, 88, 015004
- DESI Collaboration 2025, *Physical Review D*, 112, 083515
- Desmond H., 2023, *MNRAS*, 526, 3342
- Desmond H., Hees A., Famaey B., 2024, *MNRAS*, 530, 1781
- Dey A., et al., 2019, *AJ*, 157, 168
- Di Paolo C., Salucci P., Erkurt A., 2019, *MNRAS*, 490, 5451
- Di Valentino E., et al., 2025, *Physics of the Dark Universe*, 49, 101965
- Ding Q., Nakama T., Wang Y., 2020, *Science China Physics, Mechanics, and Astronomy*, 63, 290403
- Dodelson S., Widrow L. M., 1994, *Physical Review Letters*, 72, 17
- Driver S. P., et al., 2009, *Astronomy & Geophysics*, 50, 5.12
- Driver S. P., et al., 2022, *MNRAS*, 515, 2138
- Durakovic A., Skordis C., 2024, *JCAP*, 2024, 040
- Eckert D., Ettori S., Pointecouteau E., van der Burg R. F. J., Loubser S. I., 2022, *A&A*, 662, A123
- Efstathiou G., Sutherland W. J., Maddox S. J., 1990, *Nature*, 348, 705
- Einstein A., 1915, *Sitzungsberichte der Königlich Preußischen Akademie der Wissenschaften (Berlin)*, 6, 844
- Eisenstein D. J., Hu W., 1998, *ApJ*, 496, 605
- Eisenstein D. J., Hut P., 1998, *ApJ*, 498, 137
- Ettori S., Donnarumma A., Pointecouteau E., Reiprich T. H., Giodini S., Lovisari L., Schmidt R. W., 2013, *SSR*, 177, 119
- Faber S. M., Gallagher J. S., 1979, *ARA&A*, 17, 135
- Famaey B., Binney J., 2005, *MNRAS*, 363, 603
- Famaey B., McGaugh S. S., 2012, *Living Reviews in Relativity*, 15, 10
- Famaey B., Pizzuti L., Saltas I. D., 2025, *Physical Review D*, 111, 123042
- Fermi-LAT Collaboration 2015, *Physical Review Letters*, 115, 231301
- Freedman W. L., Madore B. F., Hoyt T. J., Jang I. S., Lee A. J., Owens K. A., 2025, *ApJ*, 985, 203
- Gentile G., Famaey B., de Blok W. J. G., 2011, *A&A*, 527, A76
- Guth A. H., 1981, *Physical Review D*, 23, 347
- H0DN Collaboration 2025, preprint, *Arxiv (arXiv:2510.23823)*
- Hahn O., Abel T., 2011, *MNRAS*, 415, 2101
- Harrison E. R., 1970, *Physical Review D*, 1, 2726
- Haslbauer M., Banik I., Kroupa P., 2020, *MNRAS*, 499, 2845
- Hernandez X., 2023, *MNRAS*, 525, 1401
- Hernandez X., Cookson S., Cortés R. A. M., 2022, *MNRAS*, 509, 2304
- Hernandez X., Verteletskiy V., Nasser L., Aguayo-Ortiz A., 2024a, *MNRAS*, 528, 4720
- Hernandez X., Chae K.-H., Aguayo-Ortiz A., 2024b, *MNRAS*, 533, 729
- Hinshaw G., et al., 2013, *ApJS*, 208, 19
- Hockney R. W., Hohl F., 1969, *AJ*, 74, 1102
- Hoekstra H., Jain B., 2008, *Annual Review of Nuclear and Particle Science*, 58, 99
- Hohl F., 1971, *ApJ*, 168, 343
- Hoof S., Geringer-Sameth A., Trotta R., 2020, *JCAP*, 2, 0112
- Hu W., Dodelson S., 2002, *ARA&A*, 40, 171
- Hu X.-S., Zhu B.-Y., Liu T.-C., Liang Y.-F., 2024a, *Physical Review D*, 109, 063036
- Hu J. P., Hu J., Jia X. D., Gao B. Q., Wang F. Y., 2024b, *A&A*, 689, A215
- Hu J. P., Jia X. D., Hu J., Wang F. Y., 2024c, *ApJL*, 975, L36
- Jeans J. H., 1902, *Philosophical Transactions of the Royal Society of London Series A*, 199, 1
- Jensen J. B., Blakeslee J. P., Cantiello M., Cowles M., Anand G. S., Tully R. B., Kourkchi E., Raimondo G., 2025, *ApJ*, 987, 87
- KATRIN Collaboration 2025, *Nature*, 648, 70
- Kahn F. D., Woltjer L., 1959, *ApJ*, 130, 705
- Kalbouneh B., Marinoni C., Bel J., 2023, *Physical Review D*, 107, 023507
- Karukes E. V., Salucci P., 2017, *MNRAS*, 465, 4703
- Katrin Collaboration 2019, *Physical Review Letters*, 123, 221802
- Katrin Collaboration 2022, *Nature Physics*, 18, 160
- Katrin Collaboration 2025, *Science*, 388, 180
- Katz H., McGaugh S., Teuben P., Angus G. W., 2013, *ApJ*, 772, 10
- Keenan R. C., Barger A. J., Cowie L. L., 2013, *ApJ*, 775, 62
- Keenan R. C., Barger A. J., Cowie L. L., 2016, *Proceedings of the International Astronomical Union*, 11, 295
- Kelleher R., Lelli F., 2024, *A&A*, 688, A78
- Kirilova D., Panayotova M., Chizhov E., 2024, *Symmetry*, 16, 53
- Kogut A., et al., 1993, *ApJ*, 419, 1
- Kroupa P., Pflamm-Altenburg J., Mazurenko S., Wu W., Thies I., Jadhav V., Jerabkova T., 2024, *ApJ*, 970, 94
- LUX Collaboration 2017, *Physical Review Letters*, 118, 021303
- Lelli F., McGaugh S. S., Schombert J. M., 2016, *AJ*, 152, 157
- Lelli F., McGaugh S. S., Schombert J. M., Pawlowski M. S., 2017, *ApJ*, 836, 152
- Lewis A., Challinor A., Lasenby A., 2000, *ApJ*, 538, 473
- Li P., Lelli F., McGaugh S., Schombert J., 2018, *A&A*, 615, A3
- Li P., et al., 2023, *A&A*, 677, A24
- Li P., et al., 2024, *A&A*, 692, A253
- Lopez A. M., Clowes R. G., Williger G. M., 2022, *MNRAS*, 516, 1557
- Lopez A. M., Clowes R. G., Williger G. M., 2024, *JCAP*, 2024, 055
- Ludlow A. D., et al., 2017, *Physical Review Letters*, 118, 161103
- Lüghausen F., Famaey B., Kroupa P., 2015, *Canadian Journal of Physics*, 93, 232
- Lux-Zeplin Collaboration 2023, *Physical Review Letters*, 131, 041002
- Mahmud Saad S., Ting Y.-S., 2025, preprint, *Arxiv (arXiv:2512.19652)*
- Makarov V. V., 2026, *AJ*, 171, 79
- Manchanda D., Sutherland W., Pittordis C., 2023, *The Open Journal of Astrophysics*, 6, E2
- Martel H., Shapiro P. R., 1998, *MNRAS*, 297, 467
- Mateo M. L., 1998, *ARA&A*, 36, 435
- Mazurenko S., Banik I., Kroupa P., Haslbauer M., 2024, *MNRAS*, 527, 4388
- Mazurenko S., Banik I., Kroupa P., 2025, *MNRAS*, 536, 3232
- McGaugh S., 2020, *Galaxies*, 8, 35
- McGaugh S., Lelli F., Schombert J., 2016, *Physical Review Letters*, 117, 201101
- McGaugh S. S., Lelli F., Schombert J. M., Li P., Visgaitis T., Parker K. S., Pawlowski M. S., 2021, *AJ*, 162, 202
- McGaugh S. S., Schombert J. M., Lelli F., Franck J., 2024, *ApJ*, 976, 13
- Menanteau F., et al., 2010, *ApJ*, 723, 1523
- Menanteau F., et al., 2012, *ApJ*, 748, 7
- Meszáros P., 1974, *A&A*, 37, 225
- MicroBooNE collaboration 2025, *Nature*, 648, 64
- Migkas K., Reiprich T. H., 2018, *A&A*, 611, A50
- Migkas K., Pacaud F., Schellenberger G., Erler J., Nguyen-Dang N. T., Reiprich T. H., Ramos-Ceja M. E., Lovisari L., 2021, *A&A*, 649, A151
- Milgrom M., 1983, *ApJ*, 270, 365
- Milgrom M., 2010, *MNRAS*, 403, 886
- Miller R. H., Prendergast K. H., 1968, *ApJ*, 151, 699
- Mistele T., McGaugh S., Lelli F., Schombert J., Li P., 2024a, *ApJL*, 969, L3
- Mistele T., McGaugh S., Lelli F., Schombert J., Li P., 2024b, *JCAP*, 2024, 020
- Moe M., Di Stefano R., 2017, *ApJS*, 230, 15
- Murray S. G., Robotham A. S. G., Power C., 2018, *ApJ*, 855, 5
- Nagesh S. T., Banik I., Thies I., Kroupa P., Famaey B., Wittenburg N., Parziale R., Haslbauer M., 2021, *Canadian Journal of Physics*, 99, 607
- Natarajan P., Williams L. L. R., Bradač M., Grillo C., Ghosh A., Sharon K., Wagner J., 2024, *SSR*, 220, 19
- Nusser A., 2002, *MNRAS*, 331, 909
- Nusser A., 2016, *MNRAS*, 455, 178
- Ostriker J. P., Peebles P. J. E., 1973, *ApJ*, 186, 467
- Ostriker J. P., Steinhardt P. J., 1995, *Nature*, 377, 600
- Ostriker J. P., Peebles P. J. E., Yahil A., 1974, *ApJ*, 193, L1
- Peebles P. J. E., 2022, *Annals of Physics*, 447, 169159
- Pittordis C., Sutherland W., 2023, *The Open Journal of Astrophysics*, 6, 4
- Pittordis C., Sutherland W., Shepherd P., 2025, *The Open Journal of Astrophysics*, 8, 109
- Planck Collaboration VI 2020, *A&A*, 641, A6
- Pointecouteau E., Silk J., 2005, *MNRAS*, 364, 654
- Power C., Robotham A. S. G., Obreschko D., Hobbs A., Lewis G. F., 2016, *MNRAS*, 462, 474
- Riess A. G., Breuval L., 2024, in de Grijs R., Whitelock P. A.,

- Catelan M., eds, IAU Symposium Vol. 376, IAU Symposium. Cambridge University Press, pp 15–29 ([arXiv:2308.10954](https://arxiv.org/abs/2308.10954)), [doi:10.1017/S1743921323003034](https://doi.org/10.1017/S1743921323003034)
- Riess A. G., et al., 2024, *ApJ*, **977**, 120
- Roberts M. S., Rots A. H., 1973, *A&A*, **26**, 483
- Roberts M. S., Whitehurst R. N., 1975, *ApJ*, **201**, 327
- Rogstad D. H., Shostak G. S., 1972, *ApJ*, **176**, 315
- Rubin V. C., Ford Jr. W. K., 1970, *ApJ*, **159**, 379
- Sah A., Rameez M., Sarkar S., Tsagas C. G., 2025, *European Physical Journal C*, **85**, 596
- Said K., et al., 2025, *MNRAS*, **539**, 3627
- Samaras N., Grandis S., Kroupa P., 2025, *MNRAS*, **541**, 784
- San Martín M., Rubio C., 2023, *Annals of Physics*, **458**, 169444
- Sanders R. H., 1998, *MNRAS*, **296**, 1009
- Sanders R. H., 1999, *ApJ*, **512**, L23
- Sanders R. H., 2001, *ApJ*, **560**, 1
- Sanders R. H., 2003, *MNRAS*, **342**, 901
- Sanders R. H., 2008, *MNRAS*, **386**, 1588
- Sawala T., Teeriaho M., Frenk C. S., Helly J., Jenkins A., Racz G., Schaller M., Schaye J., 2025, preprint, *Arxiv* ([arXiv:2502.03515](https://arxiv.org/abs/2502.03515))
- Schaye J., et al., 2015, *MNRAS*, **446**, 521
- Scolnic D., et al., 2025, *ApJL*, **979**, L9
- Sereno M., et al., 2025, *A&A*, **693**, A2
- Shanks T., Hogarth L. M., Metcalfe N., 2019a, *MNRAS*, **484**, L64
- Shanks T., Hogarth L. M., Metcalfe N., Whitbourn J., 2019b, *MNRAS*, **490**, 4715
- Shelest A., Lelli F., 2020, *A&A*, **641**, A31
- Silk J., 1968, *ApJ*, **151**, 459
- Simon J. D., 2019, *ARA&A*, **57**, 375
- Skordis C., Złošnik T., 2019, *Physical Review D*, **100**, 104013
- Skordis C., Złošnik T., 2021, *Physical Review Letters*, **127**, 161302
- Skordis C., Złošnik T., 2022, *Physical Review D*, **106**, 104041
- Smith B., et al., 2022, Yt Astro Analysis Version 1.1.2, Zenodo, [doi:10.5281/zenodo.5911048](https://doi.org/10.5281/zenodo.5911048)
- Smoot G. F., Gorenstein M. V., Muller R. A., 1977, *Physical Review Letters*, **39**, 898
- Sofue Y., Rubin V., 2001, *ARA&A*, **39**, 137
- Song D., Hiroshima N., Murase K., 2024, *JCAP*, **2024**, 087
- Spergel D. N., et al., 2003, *ApJS*, **148**, 175
- Spergel D. N., et al., 2007, *ApJS*, **170**, 377
- Stiskalek R., Desmond H., 2023, *MNRAS*, **525**, 6130
- Teyssier R., 2002, *A&A*, **385**, 337
- Thomas D. B., Mozaffari A., Złošnik T., 2023, *JCAP*, **2023**, 006
- Tolstoy E., Hill V., Tosi M., 2009, *ARA&A*, **47**, 371
- Tomasetti E., et al., 2025, preprint, *Arxiv* ([arXiv:2509.02692](https://arxiv.org/abs/2509.02692))
- Tremaine S., Gunn J. E., 1979, *Physical Review Letters*, **42**, 407
- Tristram M., et al., 2024, *A&A*, **682**, A37
- Tully R. B., Fisher J. R., 1977, *A&A*, **54**, 661
- Turk M. J., Smith B. D., Oishi J. S., Skory S., Skillman S. W., Abel T., Norman M. L., 2011, *ApJS*, **192**, 9
- Uddin S. A., et al., 2024, *ApJ*, **970**, 72
- Valcin D., Jimenez R., Verde L., Bernal J. L., Wandelt B. D., 2021, *JCAP*, **2021**, 017
- Valcin D., Jimenez R., Seljak U., Verde L., 2025, *JCAP*, **2025**, 030
- Vogl C., et al., 2025, *A&A*, **702**, A41
- Vokrouhlický D., Nesvorný D., Tremaine S., 2024, *ApJ*, **968**, 47
- Văraşteanu A. A., et al., 2025, *MNRAS*, **541**, 2366
- Wagenveld J. D., et al., 2024, *A&A*, **690**, A163
- Wang J., et al., 2022, *ApJ*, **936**, 161
- Watkins R., et al., 2023, *MNRAS*, **524**, 1885
- White S. D. M., Rees M. J., 1978, *MNRAS*, **183**, 341
- Whitford A. M., Howlett C., Davis T. M., 2023, *MNRAS*, **526**, 3051
- Wittenburg N., Kroupa P., Famaey B., 2020, *ApJ*, **890**, 173
- Wittenburg N., Kroupa P., Banik I., Candlish G., Samaras N., 2023, *MNRAS*, **523**, 453
- Wong J. H. W., Shanks T., Metcalfe N., Whitbourn J. R., 2022, *MNRAS*, **511**, 5742
- Xiang M., Rix H.-W., 2022, *Nature*, **603**, 599
- Xiang M., Rix H.-W., Yang H., Liu J., Huang Y., Frankel N., 2025, *Nature Astronomy*, **9**, 101
- Yasin T., Stiskalek R., Desmond H., von Hausegger S., Ferreira P. G., 2026, preprint, *Arxiv* ([arXiv:2602.06007](https://arxiv.org/abs/2602.06007))
- Zeldovich Y. B., 1972, *MNRAS*, **160**, 1P
- Zhao H., Famaey B., Lüghausen F., Kroupa P., 2013, *A&A*, **557**, L3
- Zwicky F., 1933, *Helvetica Physica Acta*, **6**, 110
- de Bernardis P., et al., 2000, *Nature*, **404**, 955

This paper has been typeset from a $\text{\TeX}/\text{\LaTeX}$ file prepared by the authors.